JGR Planets

RESEARCH ARTICLE
10.1029/2023JE007835

Special Section:
ExoMars Trace Gas Orbiter - One Martian Year of Science

Martian Atmospheric Aerosols Composition and Distribution Retrievals During the First Martian Year of NOMAD/TGO Solar Occultation Measurements: 2. Extended Results, End of MY 34 and First Half of MY 35

Aurélien Stolzenbach[1], Miguel-Angel López Valverde[1], Adrian Brines[1], Ashimananda Modak[1], Bernd Funke[1], Francisco González-Galindo[1], Ian Thomas[2], Giuliano Liuzzi[3], Gerónimo Villanueva[4], Mikhail Luginin[5], Shohei Aoki[2,6], Udo Grabowski[7], José Juan Lopez Moreno[1], Julio Rodriguez-Gomez[1], Mike Wolff[8], Bojan Ristic[2], Frank Daerden[2], Giancarlo Bellucci[9], Manish Patel[10], and Ann-Carine Vandaele[2]

[1]Instituto de Astrofísica de Andalucia, Granada, Spain, [2]Belgian Royal Institute for Space Aeronomy, Brussels, Belgium, [3]School of Engineering, University of Basilicata, Potenza, Italy, [4]NASA Goddard Space Flight Center, Greenbelt, MD, USA, [5]Space Research Institute (IKI), Moscow, Russia, [6]Japan Aerospace Exploration Agency (JAXA), Tokyo, Japan, [7]Karlsruhe Institute of Technology, Institute of Meteorology and Climate Research, Karlsruhe, Germany, [8]Space Science Institute, Boulder, CO, USA, [9]Institute for Space Astrophysics and Planetology, Roma, Italy, [10]Open University, Milton Keynes, UK

Key Points:

- MY 34 C-Storm aerosol effective size and vertical structure is similar to MY 34 Global Dust Storm (GDS)
- MY 35 early dust event aerosol shows similar effective size and vertical structure as MY 34 GDS
- MY 34 GDS leads to more intense C-Storm and an unusual early storm at the start of MY 35

Correspondence to:
A. Stolzenbach,
aurelien.stolzenbach@gmail.com

Citation:
Stolzenbach, A., López Valverde, M.-A., Brines, A., Modak, A., Funke, B., González-Galindo, F., et al. (2023). Martian atmospheric aerosols composition and distribution retrievals during the first Martian year of NOMAD/TGO solar occultation measurements: 2. Extended results, end of MY 34 and first half of MY 35. *Journal of Geophysical Research: Planets*, *128*, e2023JE007835. https://doi.org/10.1029/2023JE007835

Received 21 MAR 2023
Accepted 16 OCT 2023

Abstract This is the second part of Stolzenbach et al. (2023, https://doi.org/10.1029/2022JE007276), named hereafter Paper I, extends the period to the end of MY 34 and the first half of MY 35. This encompasses the end phase of the MY 34 Global Dust Storm (GDS), the MY 34 C-Storm, the Aphelion Cloud Belt (ACB) season of MY 35, and an unusual early dust event of MY 35 from L_S 30° to L_S 55°. The end of MY 34 overall aerosol size distribution shows the same parameters for dust and water ice to what was seen during the MY 34 GDS. Interestingly, the layered water ice vertical structure of MY 34 GDS disappears. The MY 34 C-Storm maintains condition like the MY 34 GDS. A high latitude layer of bigger water ice particles, close to 1 μm, is seen from 50 to 60 km. This layered structure is linked to an enhanced meridional transport characteristic of high intensity dust event which put the MY 34 C-Storm as particularly intense compared to non-GDS years C-Storms as previously suggested by Holmes et al. (2021, https://doi.org/10.1016/j.epsl.2021.117109). Surprisingly, MY 35 began with an unusually large dust event (Kass et al., 2020, https://ui.adsabs.harvard.edu/abs/2020AGUFMP039…01K) found in the Northern hemisphere during L_S 35° to L_S 50°. During this dust event, the altitude of aerosol first detection is roughly equal to 20 km. This is close to the values encountered during the MY 34 GDS, its decay phase and the C-Storm of the same year. Nonetheless, no vertical layered structure was observed.

Plain Language Summary Mars has a peculiar tendency, in one in every three Martian year, the entire planet is covered by dust suspended in the atmosphere. These events are referred as Global Dust Storms (GDS). The dust is lifted by fierce winds from the ground up to 80 km high. The mixture of water ice crystals and dust particle in the air of Mars change how the incoming Sun light warms the atmosphere. It is then of a crucial importance to properly characterize the nature and size of the aerosols, especially during a GDS, to better understand the dynamics of the Martian atmosphere. The spacecraft (ESA/Roscosmos) ExoMars Trace Gas Orbiter has been studying the Martian atmosphere since April 2018 and observed a GDS but also other and less intense dust storms. These data help us distinguish the aerosols nature (dust and water ice) and sizes during these distinct types of dust events. Our study confirms that, globally, the particles of dust and water ice are quite small, close to 1 μm or even less. Their distribution varies a lot, meaning that one may find a lot of different particle sizes or lot of similar sized particles.

1. Introduction

The first part of this article, Paper I (Stolzenbach et al., 2023), detailed the method of the Martian atmospheric composition and distribution retrieval using NOMAD-SO experiment onboard the ExoMars Trace Gas Orbiter mission (TGO) (ESA/Roscosmos) spacecraft. They studied the Martian year 34 Global Dust Storm (GDS) period (L_S 190° to L_S 260°) and described the Martian aerosol composition, vertical structure evolution in time and

location as well as the effective radius and variance (r_{eff} and ν_{eff}) which characterize the aerosol distribution. Paper I reported a general increase in aerosol content and vertical extent, both dust and water ice, during the MY 34 GDS peak intensity phase (L_S 190° to L_S 210°). During the decay phase (L_S 210° to L_S 260°), the atmospheric aerosol content and vertical extent tends to decrease. The dust r_{eff} was roughly equal to 1 μm with a ν_{eff} mainly lower than 0.2 throughout the MY 34 GDS. Water ice r_{eff} was reported to be smaller, mainly lower than 0.5 μm, but with a ν_{eff} also lower than 0.2 throughout the MY 34 GDS.

Broadly speaking, planetary atmospheres are highly influenced by the aerosol content. The impact of the aerosol nature and size distribution alter the energy budget of the atmosphere in a specific way. On Mars, mineral dust in suspension affects the atmospheric temperature through radiative heating (Davies, 1979; Forget et al., 1999; Kleinböhl et al., 2009, 2011; Smith, 2004). Whereas water ice crystals also affect temperature and water cycle through radiative equilibrium (Madeleine et al., 2012; T. Navarro et al., 2014; Wilson et al., 2008) and condensation/sublimation processes (Clancy et al., 2017; Montmessin et al., 2004, 2017; Richardson & Wilson, 2002). Mars is well-known to have an active atmosphere in regards of its aerosol content. Especially, one of the most peculiar Martian events is the Global Dust Storms (referred as GDS in deference of Haberle et al. (2017)). These events are planet-encircling dust storms occurring in approximately one in 3 years and restricted seasonally to southern spring and summer (Zurek & Martin, 1993). Global Dust Storms have been studied exhaustively in the past and a list of related articles are compiled in Paper I. Understanding Mars climatology demands to characterize the interannual variability of dust events such as done by Zurek and Martin (1993), Clancy et al. (2000), Smith (2004), Montabone et al. (2015), and Kass et al. (2016). The dataset used in this paper is a recent opportunity to assess the relationships between the most recent GDS and the later dust events.

In Section 3.1 part of this article we present an overview of our results for a whole Martian year (end of MY 34 and first half of MY 35). This encompasses the MY 34 GDS which is treated in depth in Paper I. In Section 3.2 we present and discuss our results for the end of MY 34. The aerosol's composition and size during the MY 34 C-Storm (following the MY 34 GDS and starting at L_S 320°) are described in Section 3.2.2. An unusual dust event occurred from L_S 320° to L_S 320° at the beginning of MY 35 (Kass et al., 2020) is studied in Section 3.3 alongside the rest of the first half of MY 35. An emphasis in the data comparison is made with recent and similar studies from TGO experiments as shown in Luginin et al. (2020), Liuzzi et al. (2020), and Stcherbinine et al. (2020, 2022). The present article highlights the interest importance of continuous measurements during consecutive Martian years, inside/outside GDS. The insight into the aerosol vertical distribution, provided by the NOMAD-SO experiment onboard TGO, very needed to tackle the question of interannual variability of the airborne dust and water ice.

2. Methods and Data

This section will briefly present the dataset and retrieval methods. For a more detailed presentation of these aspects of our study, please refer to Paper I Sections 2–4.

2.1. NOMAD-SO Data Set and Retrieval Method

NOMAD is a suite of three spectrometers onboard TGO, covering the spectral ranges from the UV, the visible and the IR, from 0.2 to 4.3 μm (Vandaele et al., 2018). The instrument has one IR spectrometers working in Solar Occultation (SO channel), operating in the spectral range between 2.3 and 4.3 μm (2,320-4,350 cm^{-1}). The time sampling of this channel is approximately of 1 s, allowing for a vertical sampling of about 1 km. The Acousto-Optical Tunable Filter (AOTF) present in the instrument allows for a rapid change between diffraction orders resulting of observations in 6 different diffraction every second at a given altitude.

Our retrieval program, RCP (for Retrieval Control Program), solves iteratively the inverse problem (Rodgers, 2000) and is shortly described in Paper I and in detail in J. Navarro and Aythami (2016). RCP works in duo with the radiative forward model Karlsruhe Optimized Radiative Transfer Algorithm (KOPRA) (Stiller et al., 1998). More details about KOPRA can also be found in Paper I. Using NOMAD-SO spectrums, RCP retrieves the extinction vertical profile using a global fit and not the usual onion-peeling or Abel's transform method. This is different from earlier works on aerosols using ACS data (Luginin et al., 2020; Stcherbinine et al., 2020, 2022), who used onion-peeling method. Our fitting method follows Luginin et al. (2020). We evaluate the best set of parameters, the effective radius (r_{eff}), the effective variance (ν_{eff})

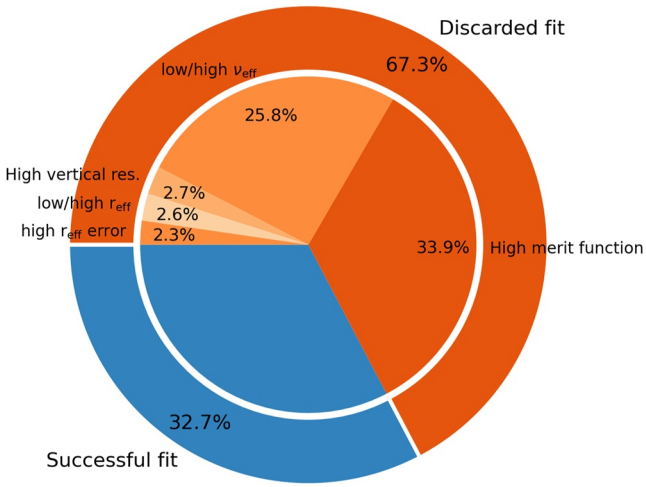

Figure 1. Statistics of the fitting procedure performance for the whole dataset.

and the ratio of the number density of water ice over the number density of dust (γ) that describes the Martian aerosol distribution at a given altitude by finding the minimum of a merit function. A full description of the fitting procedure can be found in Section 4.3 of Paper I.

2.2. Uncertainties and Filtering

We evaluate two effective variances, $\nu_{\text{eff dust}}$ and $\nu_{\text{eff H}_2\text{O ice}}$, to fit properly the extinction ratio signal. Without accounting to the possible changes in effective variance, we find that we cannot reproduce all the spectral broadband behaviors of the extinction ratio (as seen in Paper I Section 4.2). An analogous reasoning applies to the γ parameter introducing the notion of mixture, of dust and water ice, in the extinction signal. Regarding the effective variances, they are per se fixed in our final step of the fitting procedure even if we supply their uncertainties from their evaluation during the Brute Force algorithm (see Paper I Section 4.3). As mentioned in Paper I Section 4.3, we filter for $\nu_{\text{eff}} < 0.02$ because it results in quasi-monodisperse distributions and makes poor physical sense.

Figure 1 show the statistics of our fitting attempts for our entire dataset, running from MY 34 L_S 180° to MY 35 L_S 180°. In total, after we filter for low averaging kernel and low extinction (at least one extinction value lower than 1×10^{-5} km^{-1} from one diffraction order), we have 32.7% of successful fitting, 33.9% of discarded fitting due to high merit function value (>5), 25.8% of discarded fitting due to low or high effective variance, 2.7% of discarded fitting due to high vertical resolution, 2.6% of discarded fitting due to low/high effective radius and 2.3% due to high error on the effective radius. We have slightly less than a third of successful fitting attempts. This illustrate the difficulty to extract information about the aerosol's nature with only five diffraction order to cover the spectral behavior of the extinction caused by aerosols.

Sporadicity and non-retrieval of high altitudes aerosol detection Figures 4–7 shows that aerosol detection can be patchy or sporadic throughout the whole dataset at high altitude, above altitudes where we have a continuous aerosol detection (typically above 60 km). To make sense of this observation, we need to take a closer look at how the extinctions values behave in our retrievals. Our retrieval program, RCP, provide us with extinction for each individual diffraction order selected. When the change in spectral baseline does not vary much from altitude to altitude, RCP gives us low and oscillating extinctions. One example is given with the NOMAD-SO orbit ID 20180625_050514_1p0a_SO_A_E (see Figure 2 and also presented in Paper I Figure 1.) which took place during MY 34 L_S 200°, during the peak of the GDS. It shows the difference in extinction behavior between the high aerosol content altitudes (from 10 to 60 km) and the higher altitudes where the extinctions are lower and no aerosol content is *"detected"* by our fitting procedure. Above 60 km the extinctions oscillates around 0, from -1×10^{-5} km^{-1} to 1×10^{5} km^{-1}. Nonetheless, we can clearly identify a range of altitude, from 70 to 90 km, where we surely have aerosols present. Since some of the extinctions values are below 1×10^{-5} km^{-1} (and some even negatives), we filter out these altitudes. In a sense, our filtering threshold for extinctions hides potential aerosol "*detection*."If we look at Figure 3, extinctions behave a bit differently. Orbit 20190620_033502_1p0a_SO_A_I correspond to MY 35 L_S 42° without an intense dust event as the MY GDS and lower opacity at almost every altitude. We have two successful fitting, a merit function lower than 5, close to 85 km from extinctions that appears to be located in a region where extinctions mainly oscillates. Nonetheless, these two results are discarded due to an error on the effective radius too high as shown by the black dots in Figure 3. It means that, even by chance or high noise propagation through the inversion process, the fitting procedure provides such a high error associated to the effective radius that we filter out these results. In addition, we can do a quick and dirty statistical evaluation of the probability of a false positive detection. If we postulate that the extinctions, in an oscillating region, have 50% chances to be positive and then 50% chance to be greater than 1×10^{-5} km^{-1}, there is 1 over 1024 chances to have a false positive detection since we need our five diffraction orders to be positive and $>1 \times 10^{-5}$ km^{-1}. And then, this false positive detection due to randomness has to pass the fitting process with all the filters taking place (merit function, low/high ν_{eff}, high vertical resolution, low/high r_{eff} and high r_{eff} error), which decreases drastically the chances of an actual false positive fitting successful attempt (see Figure 1 for the detailed statistics of the fitting procedure) since a random arrangement of five extinction does not fit well the spectral behavior of dust and/or water ice particles. If it is nevertheless successful, our whole process has been tricked, and we have no way to discard it except a posteriori.

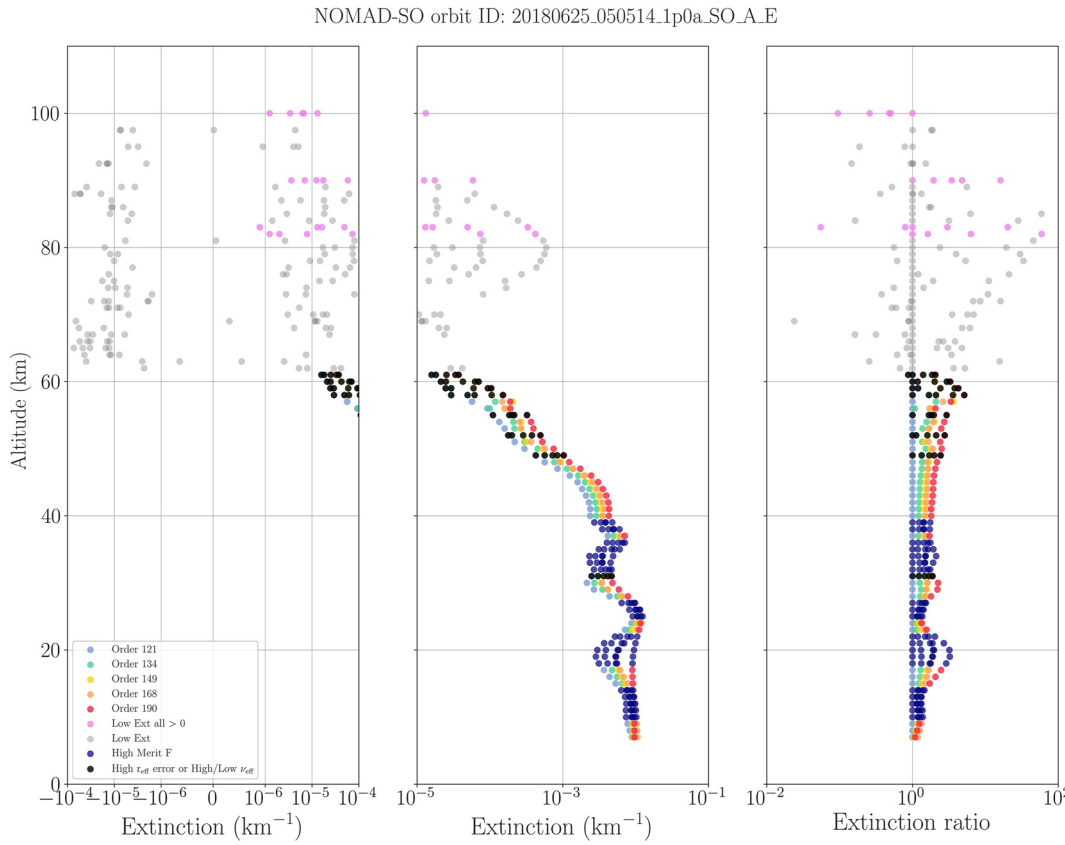

Figure 2. Extinction and extinction ratio vertical profiles for orbit 20180625_050514_1p0a_SO_A_E. Left panel: symmetrical zoom on the oscillation region (-1×10^{-5} km^{-1} to 1×10^{-5} km^{-1}). Central panel: extinction vertical profile (positive values). Right panel: Extinction ratio vertical profile with order 121 extinction as reference value. Each altitude value is colored regarding its filtered outcome after the fitting procedure. The dark blue points correspond to an altitude filtered out because of a merit function value greater that the threshold value of 5. Black points are successful fitting results (merit function <5) discarded due to a high error on the effective radius and/or a high/low effective variance. The light gray points correspond to altitude filtered out because of at least one extinction value lower than 1×10^{-5} km^{-1}. We also highlight, in light violet, altitudes where the extinctions are too low but all positive. Successful fittings are altitudes were all extinctions are colored according to their diffraction order number.

We note that the sporadic results in the upper mesosphere are representative of a specific set of extinction values. They are usually low or close the threshold fixed at 1×10^{-5} km^{-1}. This means that they are the most probable set of results to be affected by *false positive* detections despite all our filters. This also implies, for these sporadic results in the upper mesosphere, that the fitting procedure provides similar reliability as others, meaning that the merit function, vertical resolution, effective variance, effective radius and its associated error are all physically sound. That said, our *sporadic* results in the upper mesosphere are coherent with previous studies (Liuzzi et al., 2020; Luginin et al., 2020; Stcherbinine et al., 2020, 2022) with sub-micron sized water ice particles. But we also rarely find larger dust particles, which are not retrieved by any other study. We prefer to keep those results, that revised calibration and updated measurement noise of NOMAD-SO impact on our fitting procedure might discard or confirm, as they are originated from the same fitting procedure as the lower mesosphere results.

3. Results and Discussion

3.1. Overall Remarks About Our Retrieval for MY 34 and MY 35

Storms (local, rocket or global) increase the aerosol content at lower altitudes and lead to transmittance rapidly decreasing to 0 as observed by NOMAD-SO. This directly translates into poor averaging kernel for tropospheric altitudes during storms. This is shown through an increase of the altitude of aerosol first detection during storms.

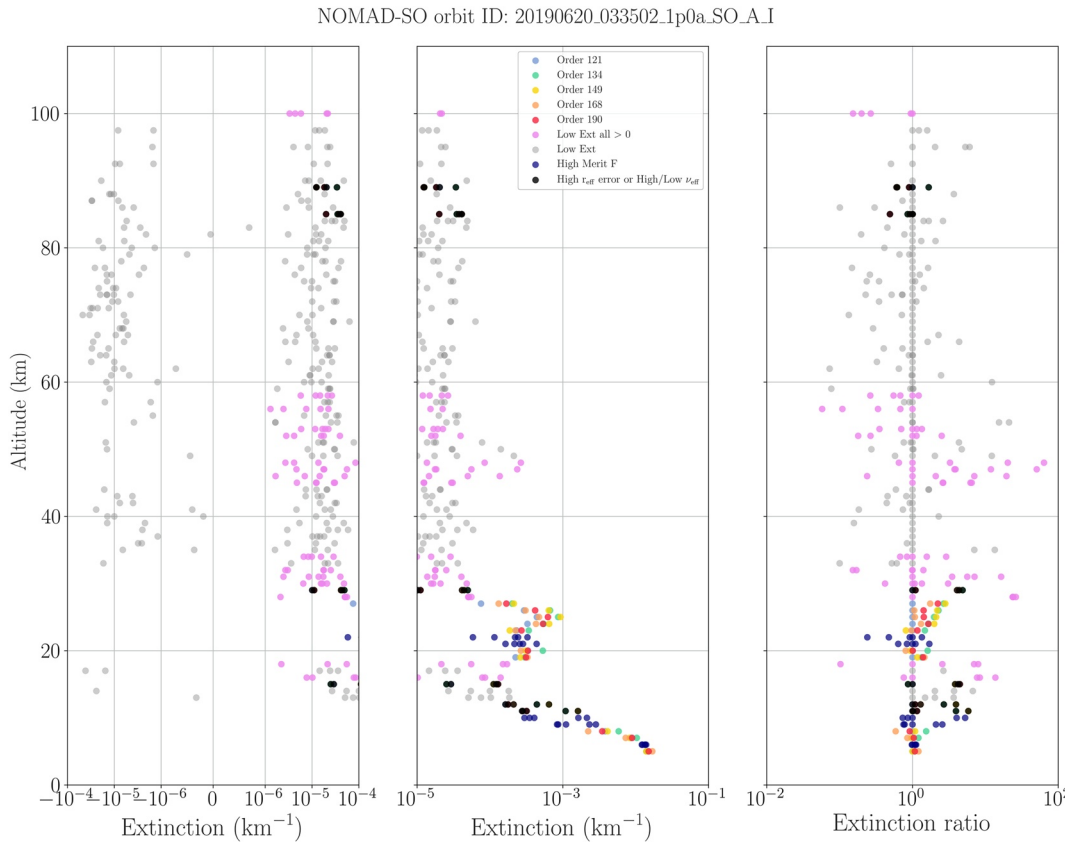

Figure 3. Extinction and extinction ratio vertical profiles for orbit 20190620_033502_1p0a_SO_A_I. Left panel: symmetrical zoom on the oscillation region (-1×10^{-5} km^{-1} to 1×10^{-5} km^{-1}). Central panel: extinction vertical profile (positive values). Right panel: Extinction ratio vertical profile with order 121 extinction as reference value. Each altitude value is colored regarding its filtered outcome after the fitting procedure. The dark blue points correspond to an altitude filtered out because of a merit function value greater that the threshold value of 5. Black points are successful fitting results (merit function <5) discarded due to a high error on the effective radius and/or a high/low effective variance. The light gray points correspond to altitude filtered out because of at least one extinction value lower than 1×10^{-5} km^{-1}. We also highlight, in light violet, altitudes where the extinctions are too low but all positive. Successful fittings are altitudes were all extinctions are colored according to their diffraction order number.

Values of the two parameters r_{eff} and ν_{eff}, the by-products $\bar{r}_g$ and the mass loading (Figures 4–7), reveal a few basic results:

- The effective radius and variance, both of dust and water ice, show a coherent behavior between the northern and southern hemisphere. This might indicate that there is no strong north-south asymmetry of the aerosol's distribution parameters.
- The effective variance, both of dust and water ice, appears to be distributed quite equally for a range of 0.1–0.5. Lower effective variance (up to 0.2) tends to be more numerous compared to larger (0.2–0.8).
- Dust effective radius shows a general bimodal behavior, with a first mode close to 1 μm and the second one, less pronounced, close to 1.8 μm. The dust effective radius is in particularly good agreement with previous study and general values reported (Clancy et al., 2003, 2019; Guzewich et al., 2014, 2019; Kahre et al., 2017; Korablev et al., 2005; Liuzzi et al., 2020; Smith et al., 2013; Wolff et al., 2006). The dusty 1.8 μm mode is representative of the lower layers where the dust 1 μm mode is representative to the upper layers. The bimodality is less pronounced when we evaluate the median radius $\bar{r}_g$. Nonetheless, dust $\bar{r}_g$ also shows some decrease with altitude, this being related to the bimodality of the effective radius from the lower to the upper layers.
- Dust $\bar{r}_g$ is in the range of 1 μm to sub-micron size with a distinct population around 0.3 μm.
- Water ice effective radius is generally below 1 μm with a peak around 0.5 μm. Nonetheless, water ice particles of a few microns are not uncommon, especially for the lower layers of the aerosol content. Our

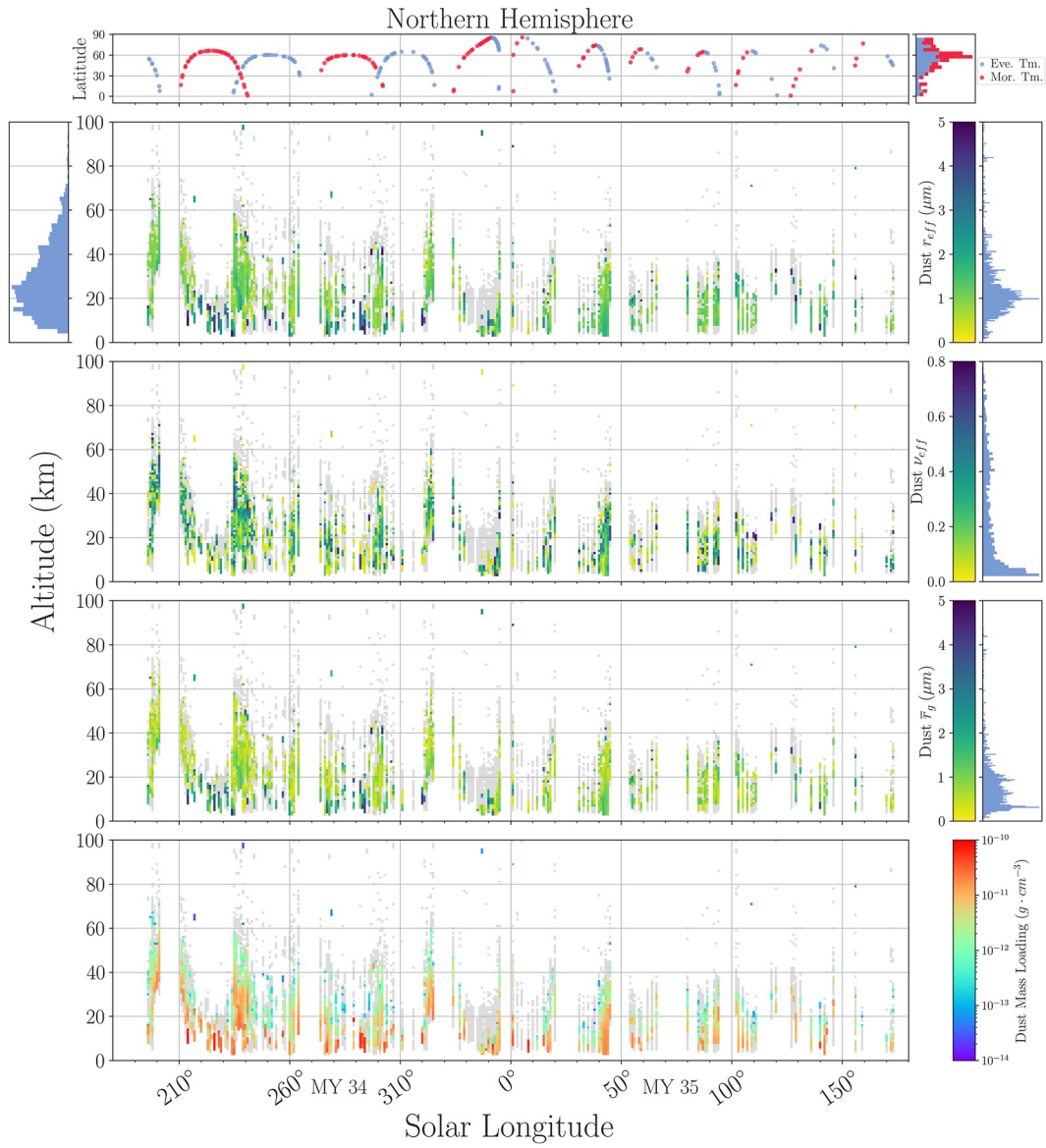

Figure 4. Results of the aerosol distribution properties analysis scheme for dust in the northern hemisphere. The filtered points (high merit function or low/high effective variance) are shown in light gray).

sub-micron water ice particles do not agree well with the common value of 2 μm generally stated (Clancy et al., 2003; Wolff & Clancy, 2003) but are consistent with more recent studies using CRISM in conjunction with MCS and MARCI observations (Clancy et al., 2019), ACS-TIRVIM (Luginin et al., 2020), ACS-MIR (Stcherbinine et al., 2020, 2022), NOMAD-SO (Liuzzi et al., 2020), and with TES observations of mesospheric aerosol (Clancy et al., 2010) which report an effective radius below 1 μm. Our discrepancy with Clancy et al. (2003) and Wolff and Clancy (2003) might come from the difference in the type of observations, namely solar occultation against Emission Phase Function (EPF) observations. Clancy et al. (2003) and Wolff and Clancy (2003) observations are from a total column point of view and so are their resulting effective size results. However, we also see a population of larger water ice particles (1–2 μm) in the troposphere that agrees better with those results.

- Water ice effective radius r_{eff} and median radius $\bar{r}_g$ decrease drastically with height. Water ice aerosols size decreases from a few microns to sub-micron particles, with most of the $\bar{r}_g$ below 0.5 μm. This transition is expected as similar variations were observed for water ice effective size in the troposphere (Guzewich

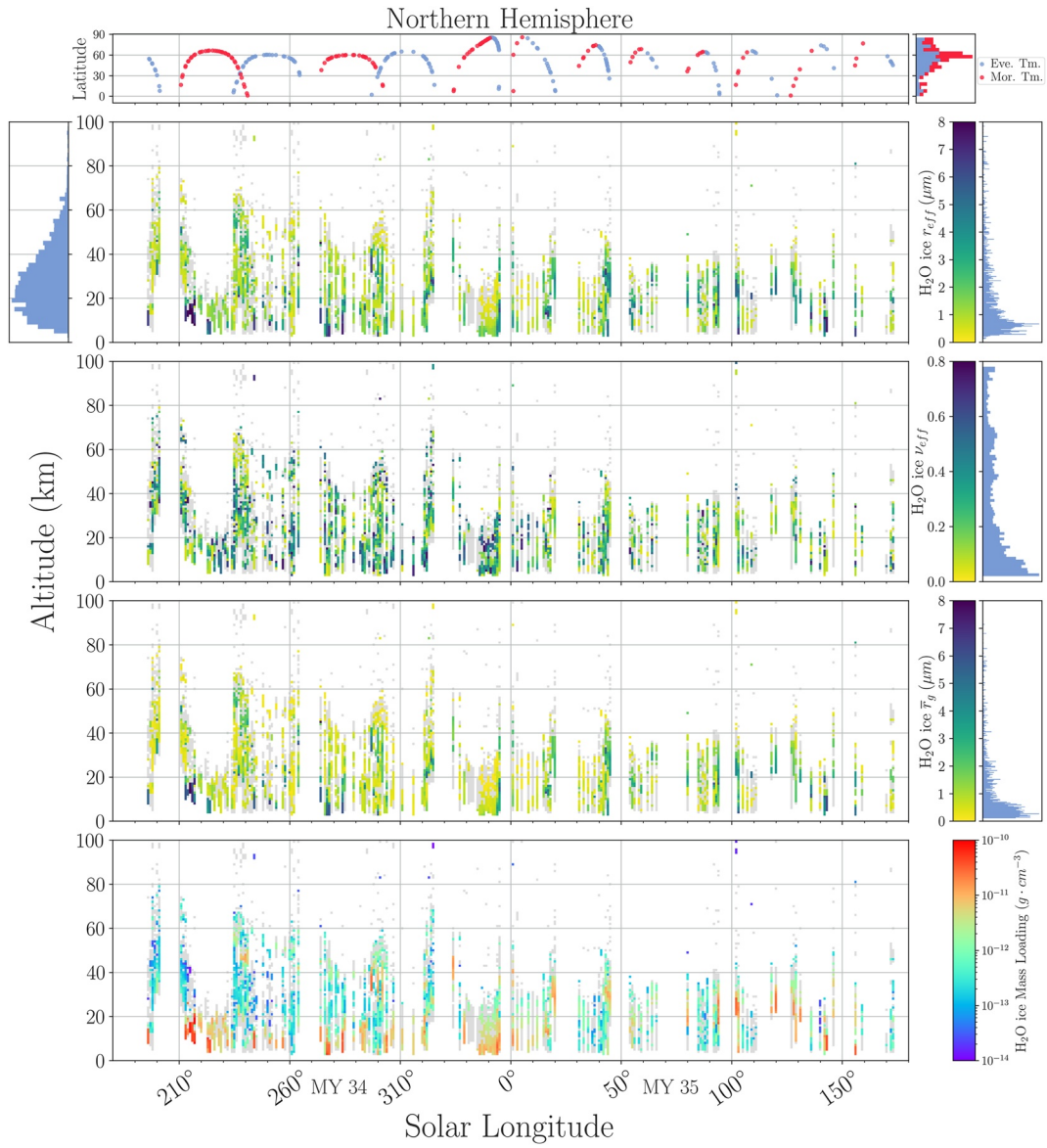

Figure 5. Results of the aerosol distribution properties analysis scheme for H_2O_{ice} in the northern hemisphere. The filtered points (high merit function or low/high effective variance) are shown in light gray).

et al., 2014; Guzewich & Smith, 2019) and the mesosphere (Clancy et al., 2019; Liuzzi et al., 2020; Luginin et al., 2020; Stcherbinine et al., 2020, 2022).

- Figure 8 shows that the effective variance of aerosols, dust, or water ice, is mostly held under $\nu_{\text{eff}} \sim 0.2$ for effective sizes greater than 2 μm. Dust aerosols of r_{eff} greater than 3 μm and water ice aerosols of r_{eff} greater than 5 μm, are mainly associated with ν_{eff} below 0.1. Bigger particles are associated with the lower layers of the aerosol content, therefore the aerosol lower layers are mainly populated with low effective variance distributions. This effective variance range is consistent with earlier studies reporting an average value of $\nu_{\text{eff}} = 0.1$ for water ice (Wolff et al. (2017) and references therein). Like recent studies using data from ACS by Luginin et al. (2020) which reported values of dust effective variance ν_{eff} of 0.1 for about 50% and of 0.2 or 0.3 for about 40% of their observations, our NOMAD results are also lower than earlier results obtained from averaged vertical column observations being in the 0.2–0.4 range (Clancy et al., 2019; Kahre et al., 2017).
- There are two distinct population for aerosol distribution with strong correlation between their effective size and variance in our results. The first one is a dust aerosol population that has a constant median radius close to 0.32 μm (see the yellow dotted line in Figure 8). This dust population exists for an effective radius range of

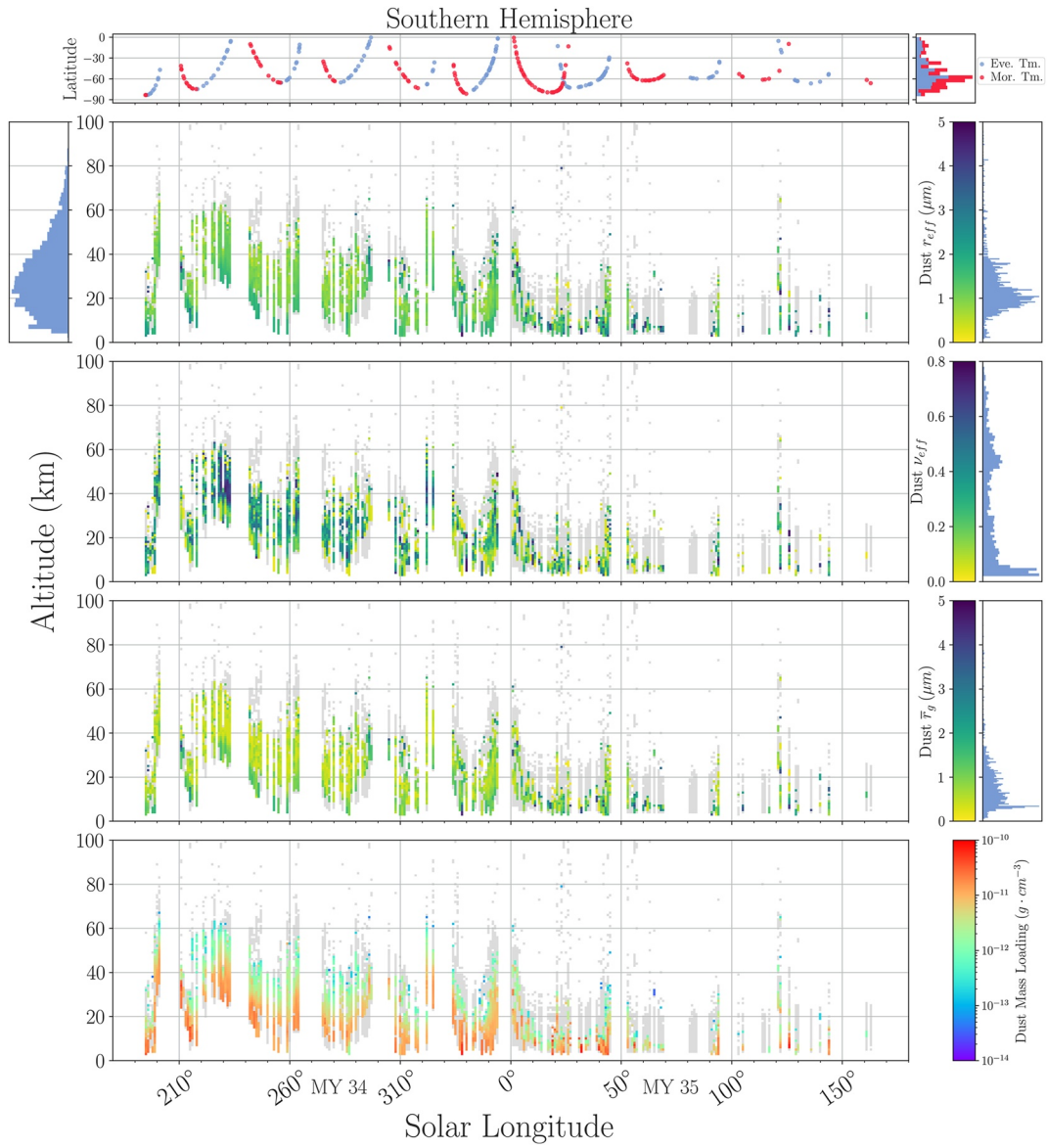

Figure 6. Results of the aerosol distribution properties analysis scheme for dust in the southern hemisphere. The filtered points (high merit function or low/high effective variance) are shown in light gray).

0.5–1.3 μm and effective variance range of 0.35–0.8. A second one is a water ice aerosol population that tends to follow a linear evolution of ν_{eff} with r_{eff} (see the dark blue line in Figure 8). This water ice population exists for an effective radius range of 0.25–1.2 μm and effective variance range of 0.35–0.8. Both populations appear to be independent of morning/evening or latitudinal correlation and are concentrated within a few kilometers in altitude. This suggests strong vertical mixing in some cloud layers with a somewhat constant aerosol size for the dust. The relationship of the linear water ice population is not straightforward and would need more inquiry. Nonetheless, as for its dusty counterpart, this behavior could suggest some specific microphysical evolution is occurring.

In addition to the previous comments, a summary of the results from Paper I and II are presented as a timeline of events during MY34 and 35 in Table 1.

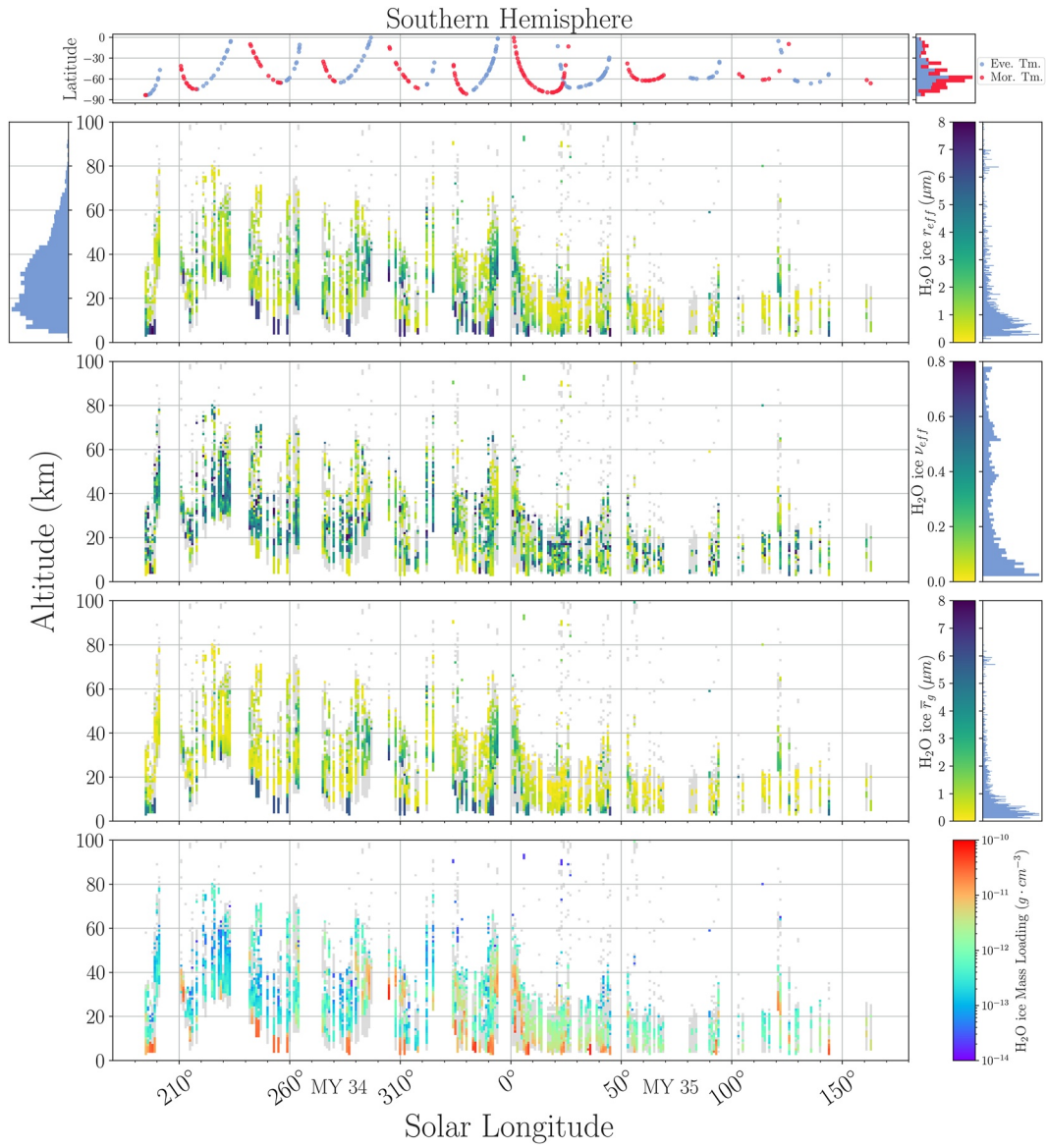

Figure 7. Results of the aerosol distribution properties analysis scheme for H_2O_{ice} in the southern hemisphere. The filtered points (high merit function or low/high effective variance) are shown in light gray).

3.2. End of the Martian Year 34

3.2.1. End of the MY 34 GDS, L_S 260° to L_S 360°

The MY 34 GDS keeps decreasing in intensity and coverage until L_S 260° even if it influences Martian atmospheric conditions until the end of MY 34. One clear aspect of this ending phase is the decrease of the altitude of aerosol first detection in our results. We see in Figures 9–12 that, for both hemispheres, the altitude of aerosol first detection is in the range of 5–10 km, except during the MY34 C-storm occurring at L_S 320°–335° (see Section 3.2.2) and for the southern mid-latitudes (up to roughly 20°S) until L_S 305° where the altitude of aerosol first detection can reach 20 km.

Aerosol size during the end of MY 34: We do not see a dramatic change in the vertical profiles of the dust effective size during the end of MY 34 compared to the peak and decay of the GDS earlier this year (see Paper I Section 5). The dust effective size vertical profiles still show a slight decrease with altitude, going from ∼2 μm in the lower layers to ∼1 μm in the upper layers. Interestingly, the averaged dust effective size vertical profile in

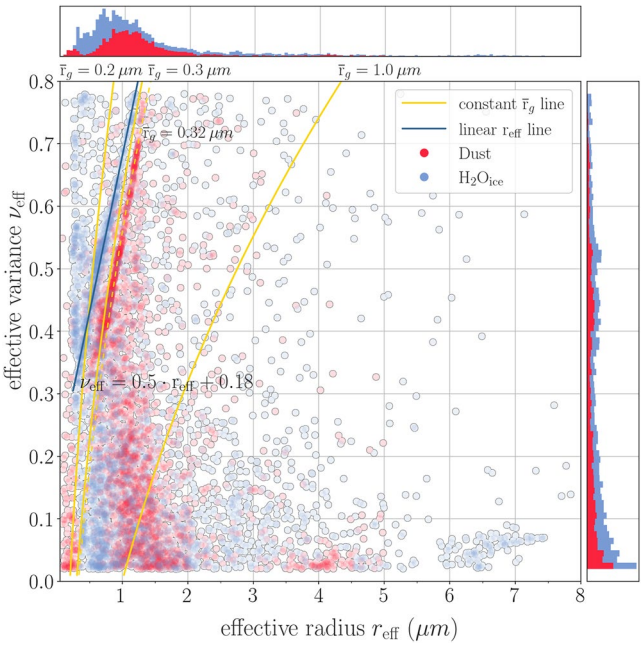

Figure 8. Scatter plot of the dust and water ice effective variance (ν_{eff}) against the effective radius (r_{eff}). Isolines with constant median radius $\bar{r}_g$ of interest are drawn in yellow. A specific linear evolution of ν_{eff} with r_{eff} is shown in dark blue.

the equatorial band shows a layer of larger dust particles around 40 km. This layer is even more pronounced if we look at the dust size in Figure 14. This layer situated at 40 km has a dust particle median radius between 3 and 4 μm for the period of equatorial observations between L_S 290° and 310° (Figures 9 and 11). Lower dust particle median radius, around 1 μm, is found for the later period of equatorial observations between L_S 320° and 360°. This is coherent with a decreasing transport intensity since the final stage of the GDS in the equatorial region around L_S 260°. The equatorial orbits scanned by TGO at $L_S \sim 295°$ (Figures 9 and 11) display a dust size of ∼ 2 μm at 40 km and the altitude range of aerosol detection covers 20–40 km. Another set of equatorial observations occur at the end of MY 34, $L_S \sim 353°$, and cover an altitude range of aerosol detection of 5–50 km but with dust effective sizes smaller around 40 km, closer to 1 μm. Averaging those two dust dataset produces the illusion of a distinct layer at 40 km while we see the final stage of the GDS decreasing intensity in the equatorial region. The vertical profiles of water ice particle sizes, effective radius (Figure 13) and median radius (Figure 14), all display the disappearance of the layered structure described earlier (see Paper I). The water ice particle size goes from 2 to 6 μm at the lowest altitude of detection depending on the latitude, to sizes from 0.1 to 1 μm at the highest altitudes. The only exception being the observations at 50°S to 70°S that took place during the MY 34 C-Storm (see Section 3.2.2). Nonetheless, water ice particles, for latitudes in the range 30°N to 50°S, are still quite large, ∼2–4 μm, up to ∼50 km. These high tropospheric micron-sized water ice clouds can be considered as a remnant of the GDS (Liuzzi et al., 2020). Stcherbinine et al. (2022) observed, using ACS-MIR data, water ice particles >2 μm at similar altitudes, location and time of year but during MY 35, period which is not described in this article. Since MY 35 is not affected by a GDS, one can argue that larger water ice particles up to ∼50 km for latitudes from 30°N to 50°S could usually be quite large at this period of each Martian year and not be correlated with any particular prior dust event.

Aerosol mass loading during the end of MY 34: The dust and water ice mass loading during the end of MY 34 (Figure 15). For the dust, the mass loading decreases from 1×10^{-11} g cm^{-1} in the lower layers to 1×10^{-12} g cm^{-1} in the upper layers. For water ice, the mass loading decreases from 1×10^{-11} g cm^{-1} in the lower layers to 1×10^{-13} g cm^{-1} in the upper layers, are quite close to those during the GDS decay phase (see Paper I). Interestingly, the water ice upper layers during the decay phase, from 40 to 60 km (see Paper I), and at the end of MY 34, from 20 to 40 km (see Figure 15) have similar particle size and mass loading. This might indicate that different atmospheric conditions (temperature, dust and water vapor content) at those two seasons lead to similar microphysical rates for water ice.

3.2.2. Inter-Annual Dust Storm Events

An inter-annual C-type dust storm (Kass et al., 2016; Smith, 2009) occurs every Martian year around L_S 320°. C-Storm usually extends in southern latitudes in the range of 30°S to 90°S with a less intense northern response constrained in latitudes of 30°N to 60°N and can also propagate to the equatorial region with even less intensity (Kass et al., 2016). Due to TGO orbit around Mars we do not have observations for the period ∼ L_S 326°–333° while the MY 34 C-Storm happened for a period of ∼ L_S 320°–336° (Holmes et al., 2021), reducing the amount of time NOMAD-SO could get data of the storm. Any dust event on Mars increases the meridional transport of water vapor to high latitudes and rises the hygropause. During the MY 34 C-Storm, the hygropause rose up to ∼70 km in the southern high latitudes, decreasing rapidly to ∼40 km toward the south pole, and up to ∼60 km in the northern hemisphere up to 60°N (Aoki et al., 2019; Fedorova et al., 2020; Holmes et al., 2021). This enhanced water vapor content at high altitude during the MY 34 C-Storm produced a distinct layer at 50–60 km in the southern hemisphere of larger water ice particles with sizes close to 1 μm in high latitudes and 3 μm in the polar region (Figure 16). Similar upper layers with larger water ice particles can be seen in the northern hemisphere but at slightly lower altitude (∼50 km) for latitudes close to 60°N (C-Storm northern response), surely due to the lower hygropause in the northern hemisphere. This vertical structure of water ice aerosol, with three layers

Table 1
Summary of the Results Organized as a Timeline of Major Dust Events

	MY 34 GDS peak		MY 34 GDS decay		End of MY 34		MY 34 C-Storm	
L_S range	L_S 190° to L_S 210°		L_S 210° to L_S 260°		L_S 260° to L_S 360°		≈L_S 320°	
areographical location	global		global		global		regional	
lowest/highest alt. of aer. detection(km)	~40 ± 10/~70 ± 10		~30 to 5/~70 ± 10		10 to 5/~40 ± 10			
layered structure	lower layers	upper layers	lower layers	upper layers	lower layers	upper layers	lower layers	upper layers
vertical extent (km)	≲50 ± 10	≳50 ± 10	≲30 ± 10	≳30 ± 10	≲20	≳20	≲30	≳30
Dust r_{eff} (μm)	1 to 2	~1	1 to 2	~1	1 to 2	~1	1 to 2	~1
H_2O_{ice} r_{eff} (μm)	≳3	≲0.3	≳3	≲0.3	≳1	≲0.3	≳1	≲0.3
Additional notes	H_2O_{ice} layer of 1–2 μm around ~60 km		H_2O_{ice} layer of 1–2 μm around ~60 km. N/S, diurnal and latitudinal asymmetry of H_2O_{ice} r_{eff}		Layer at 40 km in the equatorial region with larger dust r_{eff} of 1–4 μm. At 50 km, H_2O_{ice} with r_{eff} > 2 μm observed from 30°N to 50°		Southern regional storm with a northern response. Layer at 50–60 km of H_2O_{ice} with r_{eff} ~ 1 μm	
	MY 35 Early dust event		**MY 35 ACB**					
L_S range	L_S 30° to L_S 55°		L_S 0° to L_S 180°					
areographical location	regional, North H		equatorial band					
lowest/highest alt. of aer. detection (km)	~20/~50		~5/~40					
layered structure	lower layers	upper layers	lower layers	upper layers				
vertical extent(km)	≲20	≳20	≲20	≳20				
Dust r_{eff}(μm)	≳1	~1	≳1	≲1				
H_2O_{ice} r_{eff} (μm)	1 to 3	≲1	≳1	≲0.3				
Additional notes	Unusual dust event							

Note. For an exhaustive and detailed analysis of all the results (effective variance, median radius, mass loading, etc), the reader is referred to Paper I and Section 3 of the present article.

of distinct sizes, is typical of intense dust event as seen during the MY 34 GDS (see Paper I, Section 3.2 in this article, Liuzzi et al. (2020) and Luginin et al. (2020)). This suggests that the MY 34 C-Storm was particularly active compared to other C-Storm occurring during non-GDS year. A similar conclusion was obtained by Holmes et al. (2021) who studied the H escape during the MY 34 C-Storm.

3.3. First Half of the Martian Year 35

MY 35 is interesting to study in comparison to MY 34 and its GDS. Since the MY 34 GDS can be considered finished at the beginning of MY 35, every aerosol parameter that we retrieve can be compared with those given during MY 34, and especially during dust events.

Early dust event of MY 35, L_S 30°–55°: The first half of MY 35 presents an unusual large scale dust event L_S ~ 35° (Kass et al., 2020). This early dust event took place in the northwest of Tharsis region and developed eastward while enveloping the northern hemisphere until its end around L_S ~ 50°. The effect of this unusual northern dust event is a rising vertical extent of the aerosol content that can be seen in Figures 21 and 22 at northern latitudes ranging from 30°N to 50°N. In this range of northern latitudes, water ice particles size (Figures 21 and 22) is observed to be close to 3.5 μm from 20 to 30 km. Then, water ice size decrease upward until reaching 1 μm close to 40 km and sub-micron size for the few occurrences at mesospheric altitudes. Noticeably, the altitude

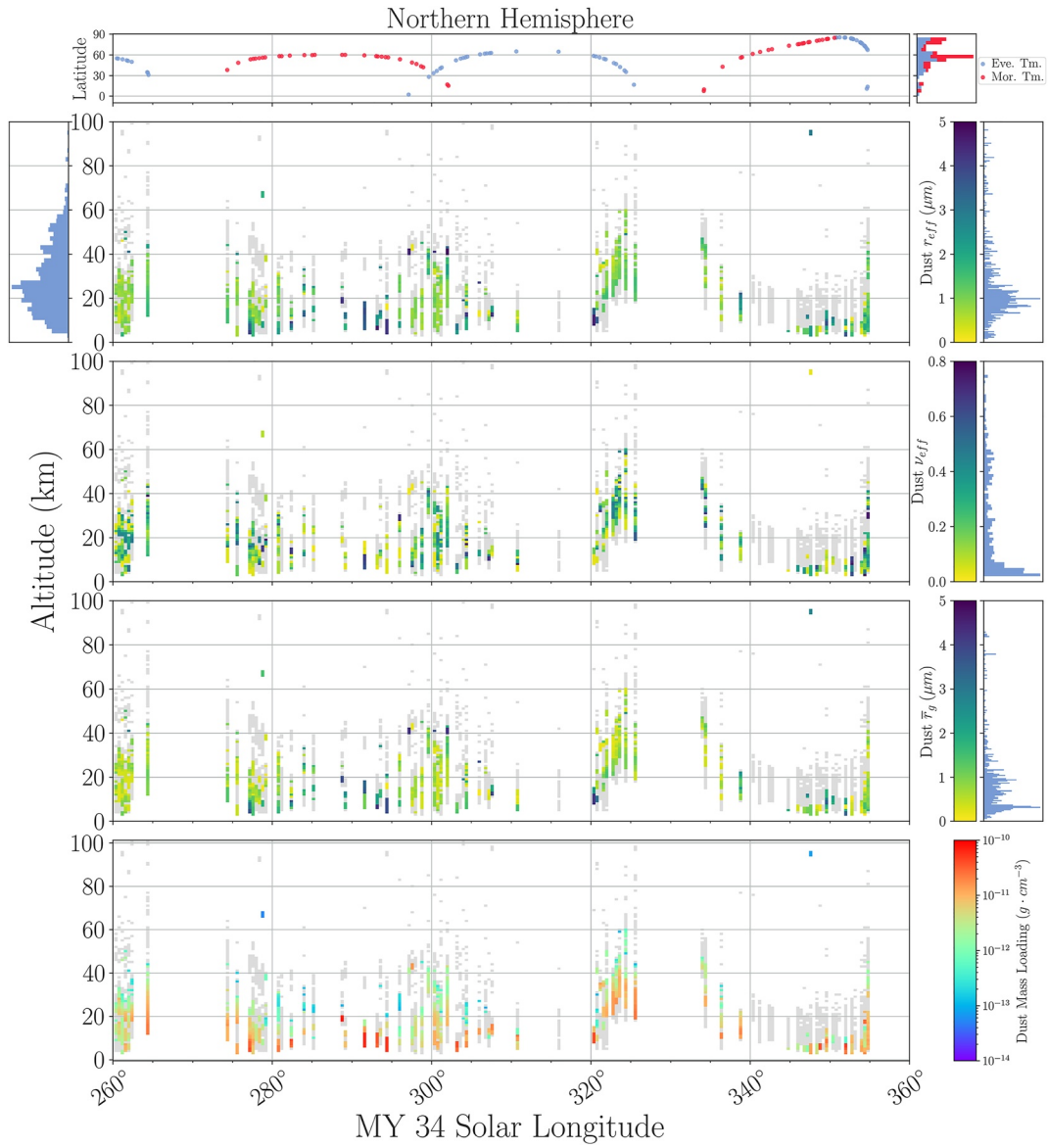

Figure 9. Results of the aerosol distribution properties analysis scheme for dust in the northern hemisphere during the end of MY34. The filtered points (high merit function or low/high effective variance) are shown in light gray).

of aerosol first detection is around 20 km which is high for the first half of MY 35 considered as a non-dusty season. Comparing to the altitude of aerosol first detection at similar latitudes during the peak of the GDS (∼30 km), its decay phase (∼20 km) and the MY 34 C-Storm (∼20 km), we can conclude that the intensity of this unusual and early dust event was comparable to the GDS decay phase and MY 34 C-Storm for this northern location. The water ice particle size in the altitude range of 20–30 km during this early event is like the water ice aerosol sizes during the GDS decay phase and MY 34 C-Storm. However, the water ice vertical profile of this early dust event does not display the larger water ice particle size upper layers seen during the MY 34 GDS decay (see Paper I) but resembles the water ice size vertical profile of MY 34 C-Storm (Figure 17).

Aphelion Cloud Belt We see a rise in altitude of the aerosol presence at low latitudes, reaching roughly 40 km while at higher latitudes it usually stops around 20 km. It can be seen in the northern hemisphere (Figures 17 and 18) at $L_S \sim 20°$, L_S 45°–55°, L_S 95°–103° and $L_S \sim 120°$ where the NOMAD observations are found at low latitudes. This greater aerosol content near the equator is typical of the Aphelion Cloud Belt (ACB) which is seen every Martian year (Clancy et al., 1996, 2017; James et al., 1996; McCleese et al., 2010). The water ice during the ACB season exhibits the same vertical behavior as seen during local storms or the peak of the GDS and the

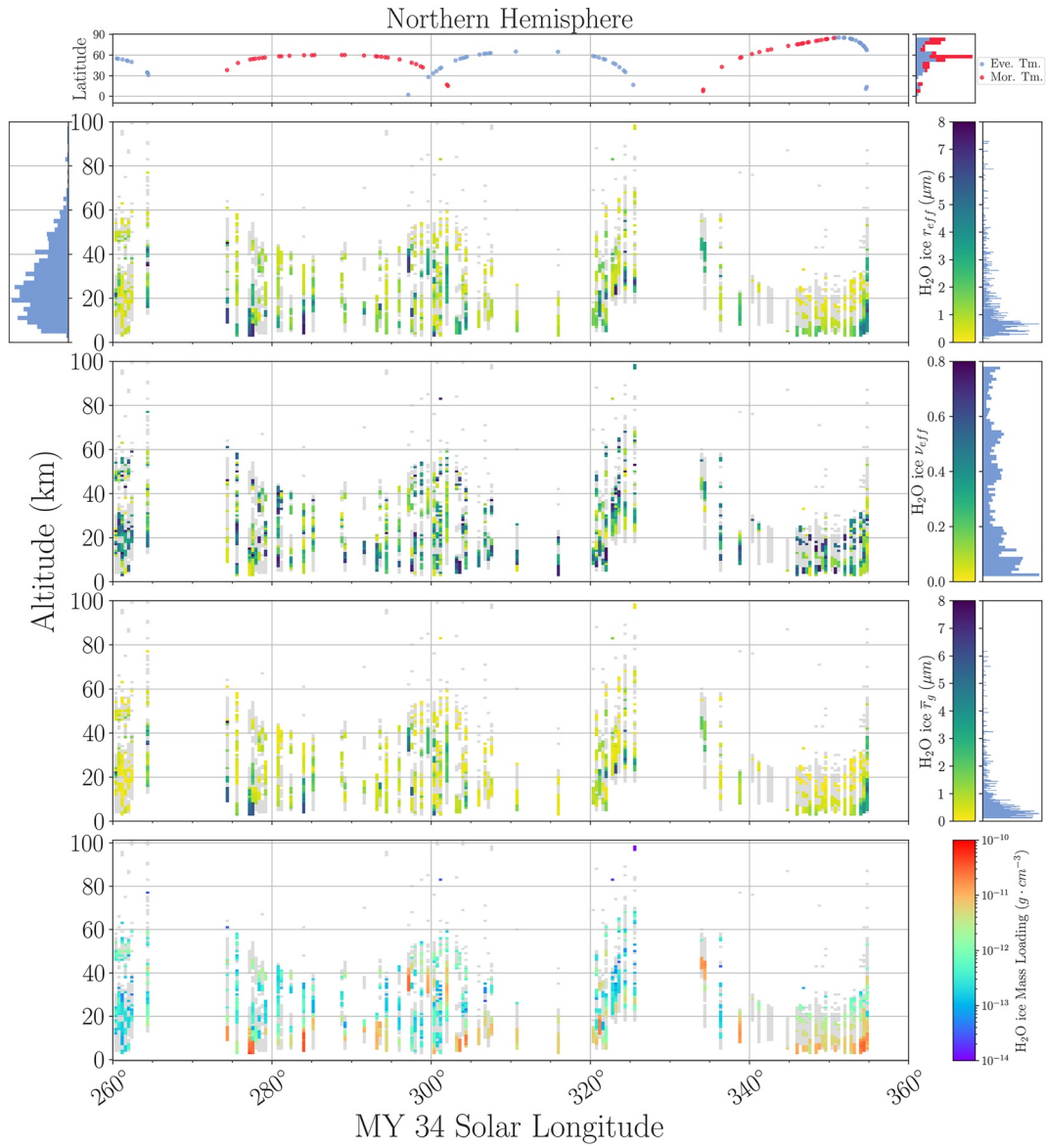

Figure 10. Results of the aerosol distribution properties analysis scheme for H_2O_{ice} in the northern hemisphere during the end of MY34. The filtered points (high merit function or low/high effective variance) are shown in light gray).

end of MY 34, with an effective radius greater in the lower layers and smaller in the upper layers. The size of the water ice particles stays mainly in the sub-micron range, only increasing toward the micron and larger for the lower layers as seen around L_S 130° in the northern hemisphere (Figure 19).

High latitudes observations Our retrieval for dust aerosols works poorly in the southern hemisphere (cf. Figure 19) for many orbits. Those filtered results are correlated with general low total amount of aerosol, with the aerosol layers restrained to altitudes <20 km. Nonetheless, the extinctions retrieved show a quasi-permanent aerosol content up to 20 km during the first half of MY 35 high latitudes in both hemispheres (Figures 17–20).

4. Conclusion

Paper I detail the method of the Martian aerosol's composition and size retrieval which follows earlier works of Luginin et al. (2020) using ACS-TIRVIM and Stcherbinine et al. (2020, 2022) using ACS-MIR.

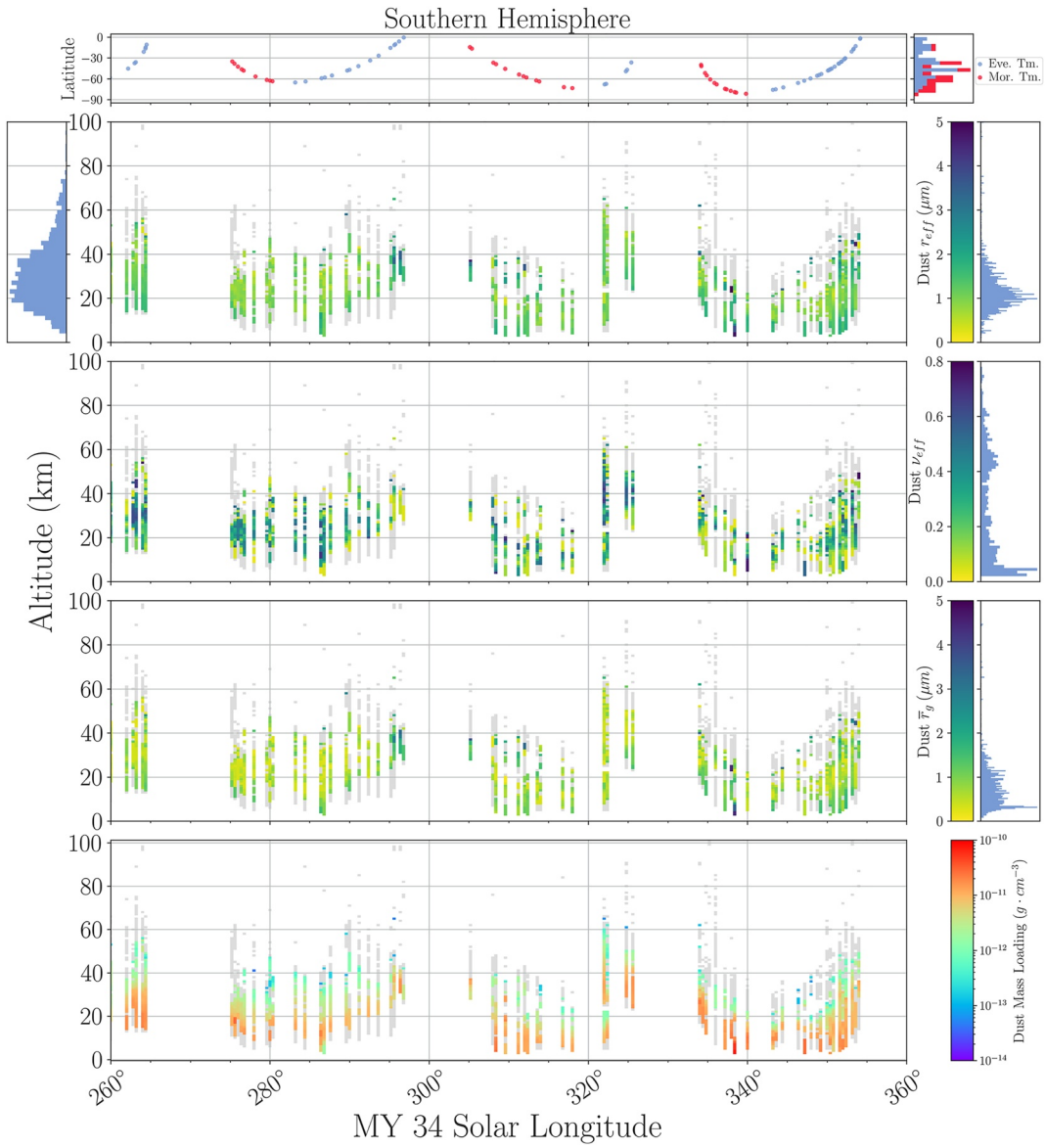

Figure 11. Results of the aerosol distribution properties analysis scheme for dust in the southern hemisphere during the end of MY34. The filtered points (high merit function or low/high effective variance) are shown in light gray).

The present article discusses the general trend of the aerosol distribution and composition throughout one full Martian year and focuses on the period following the peak of the MY 34 GDS until the end of the first half of MY 35, covering dust events such as the MY 34 C-Storm, the early dust event of MY 35 and the ACB of MY 35. We showed that the effective variance adopts a large set of values and is largely represented by values <0.2. The water ice particles are mostly <0.5 μm with micron-sized particles usually found in the lower layers of the aerosol content or in specific upper layers during the MY 34 GDS decay phase. The dust effective radius bimodal distribution centered at 1 and 1.8 μm translates to a median radius close to 1 μm with a noticeable peak at 0.3 μm. Our results of the type-C storm are in good agreement with established knowledge and especially with results from ACS (Luginin et al., 2020; Stcherbinine et al., 2020) and NOMAD-SO (Liuzzi et al., 2020). We also reported the first description of aerosol composition and vertical profiles during the unusual early dust event of MY 35 (Kass et al., 2020) which resemble to, in vertical extent and aerosol sizes, the MY 34 C-Storm even if their actual location and latitudinal coverage are not alike.

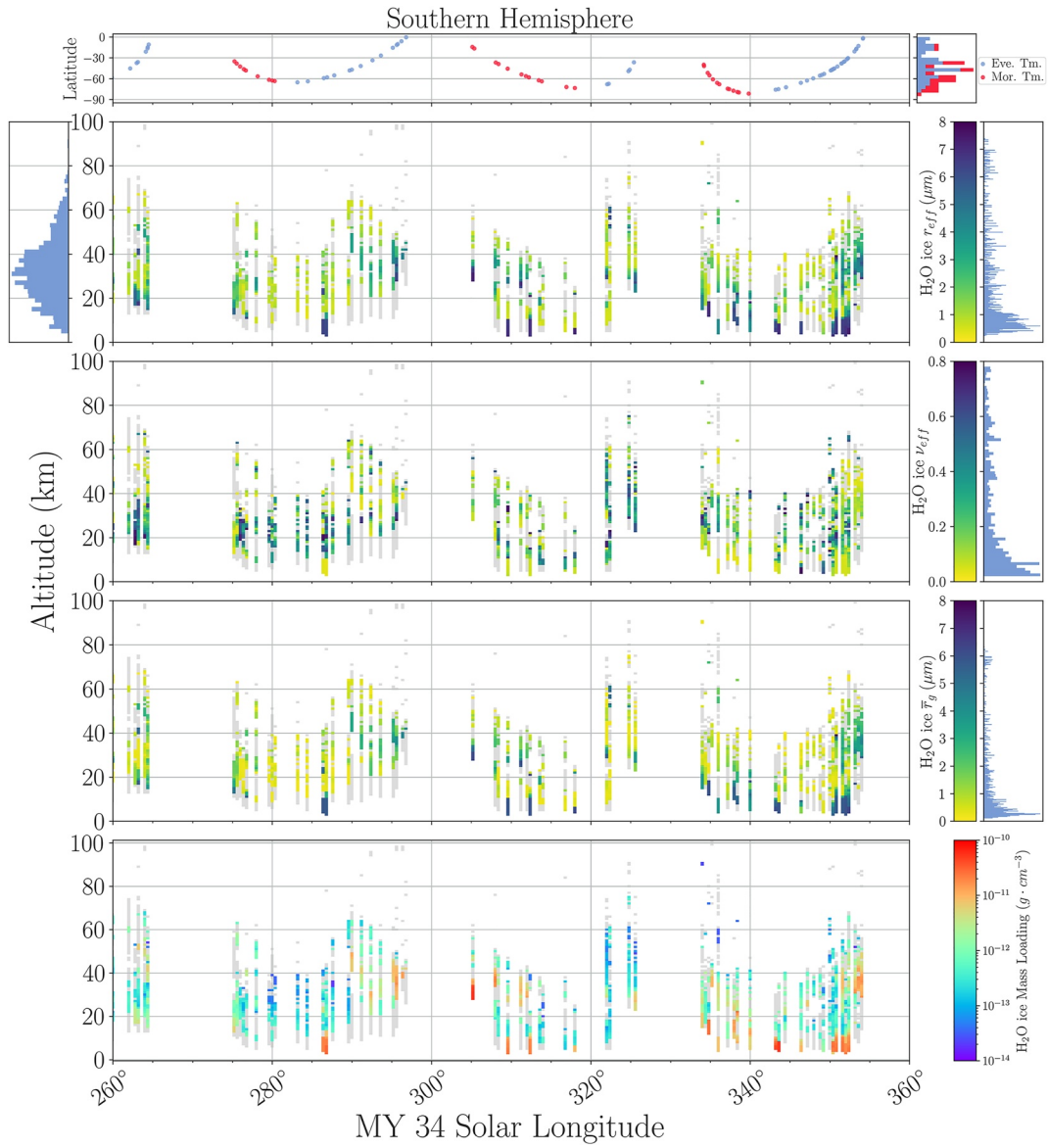

Figure 12. Results of the aerosol distribution properties analysis scheme for H_2O_{ice} in the southern hemisphere during the end of MY34. The filtered points (high merit function or low/high effective variance) are shown in light gray).

This study and its companion paper Stolzenbach et al. (2023) represent the first step at the IAA to evaluate the Martian aerosol composition and distribution using NOMAD-SO data. We plan to study in more details the available data (our selected orders represent roughly 55% of the dataset used by Liuzzi et al. (2020) for MY 34), the one presented in this general study but also NOMAD-SO data for the end of MY35 and start of MY36. We also plan to use simultaneous temperature retrieval results, as presented in López Valverde et al. (2022) which might improve the fitting process when the a priori temperature wanders far away from retrieved temperature.

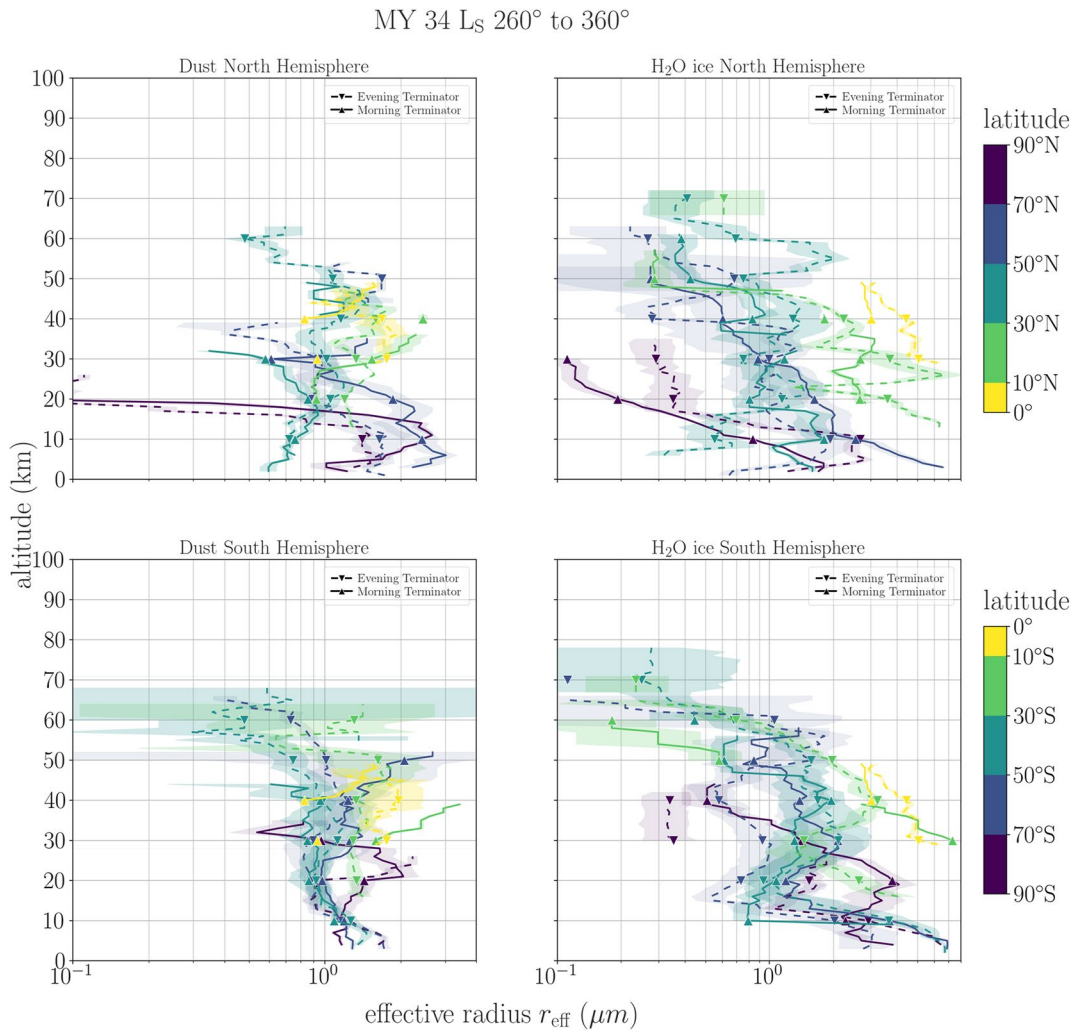

Figure 13. Vertical profiles of the effective radius during the end of MY 34. The vertical profiles are derived from a vertical running average using a vertical window of 10 km. The error displayed by the colored area is the greatest value between the standard deviation of the data points and the error evaluated during the running average.

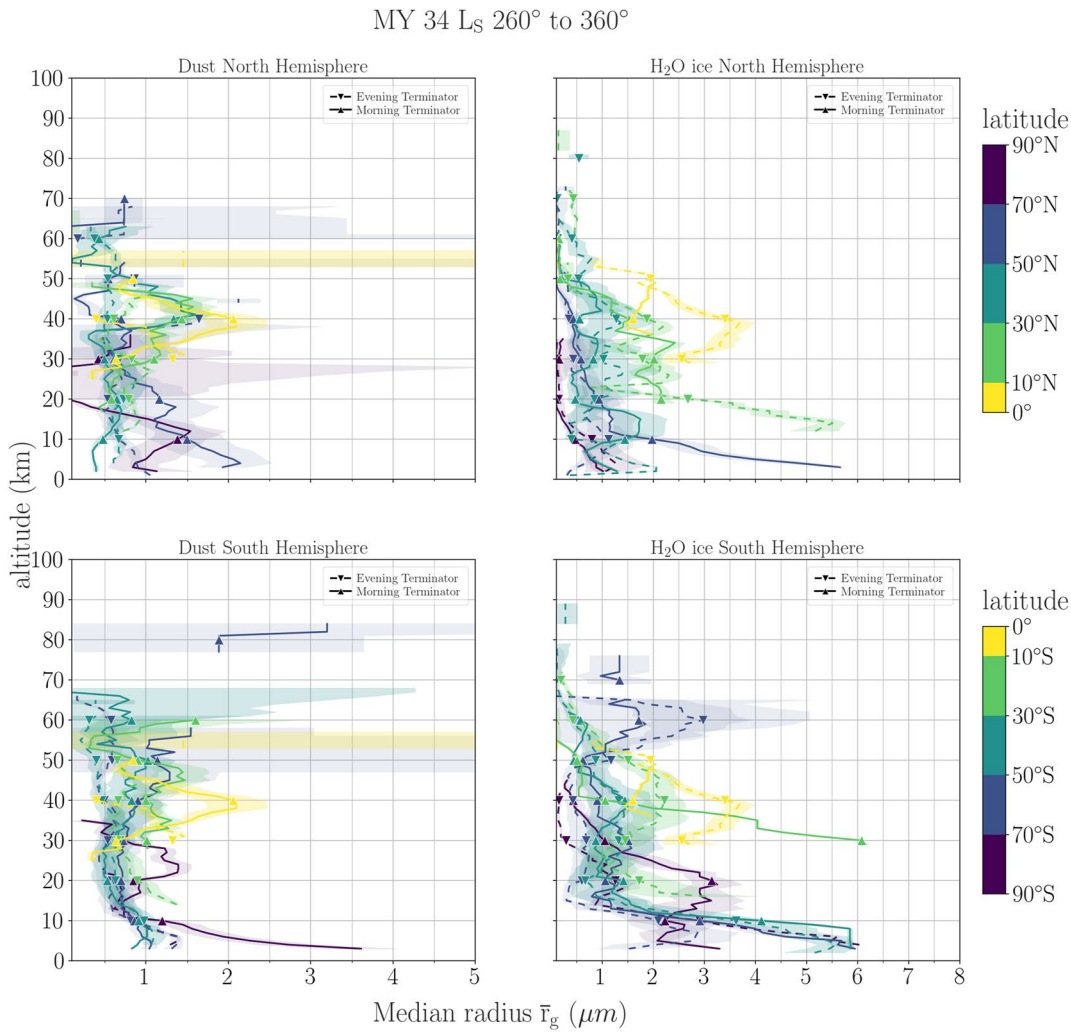

Figure 14. Vertical profiles of the median radius during the end of MY 34. The vertical profiles are derived from a vertical running average using a vertical window of 10 km. The error displayed by the colored area is the greatest value between the standard deviation of the data points and the error evaluated during the running average.

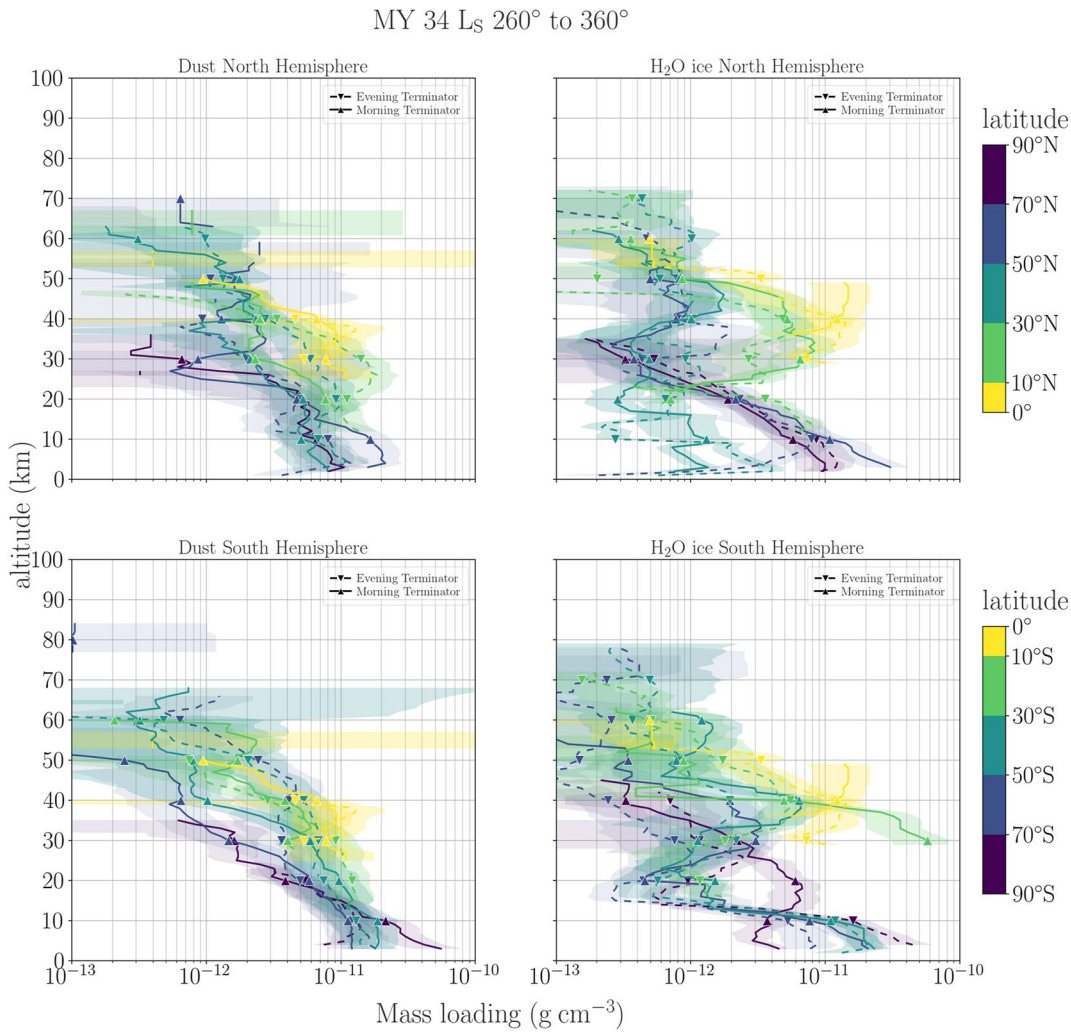

Figure 15. Vertical profiles of the mass loading during the end of MY 34. The vertical profiles are derived from a vertical running average using a vertical window of 10 km. The error displayed by the colored area is the greatest value between the standard deviation of the data points and the error evaluated during the running average.

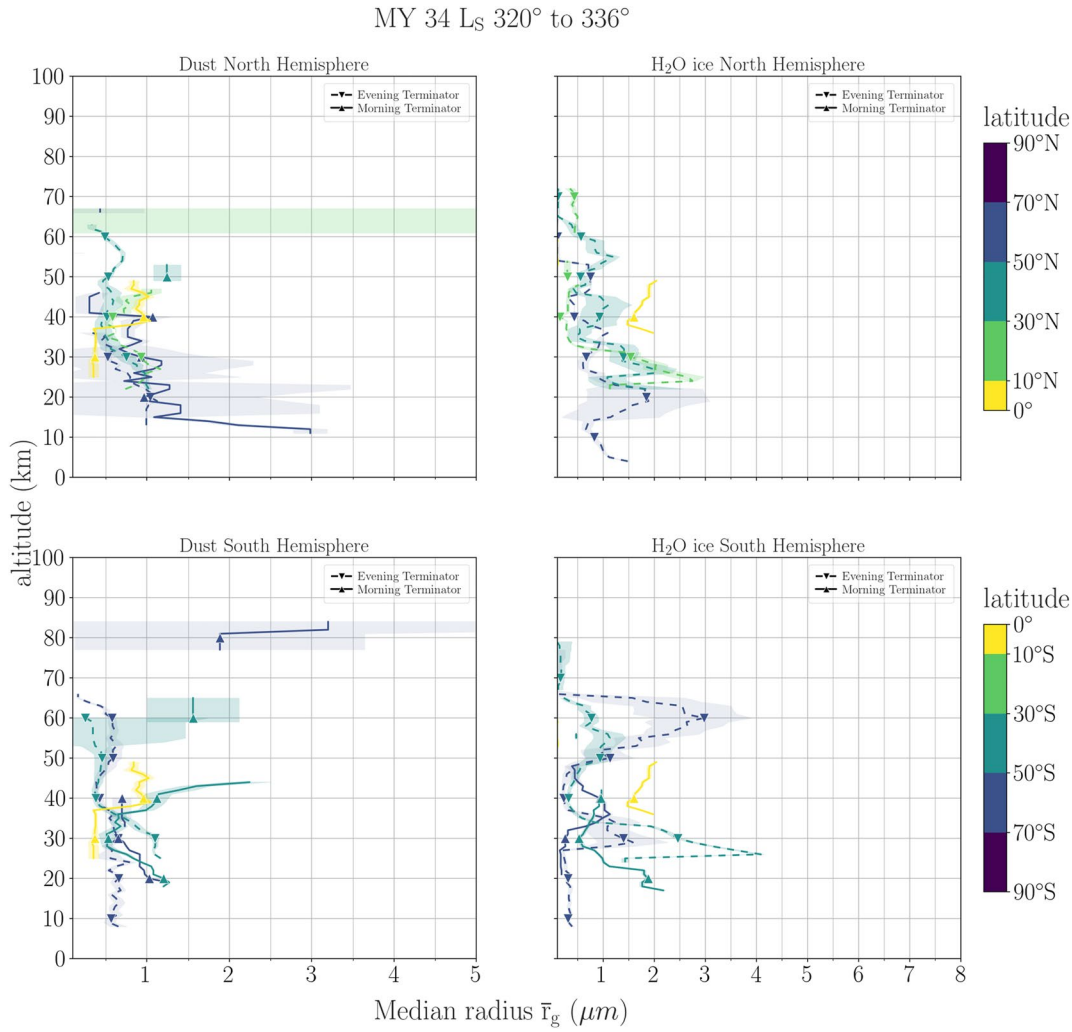

Figure 16. Vertical profiles of the median radius during the C storm. The vertical profiles are derived from a vertical running average using a vertical window of 10 km. The error displayed by the colored area is the greatest value between the standard deviation of the data points and the error evaluated during the running average.

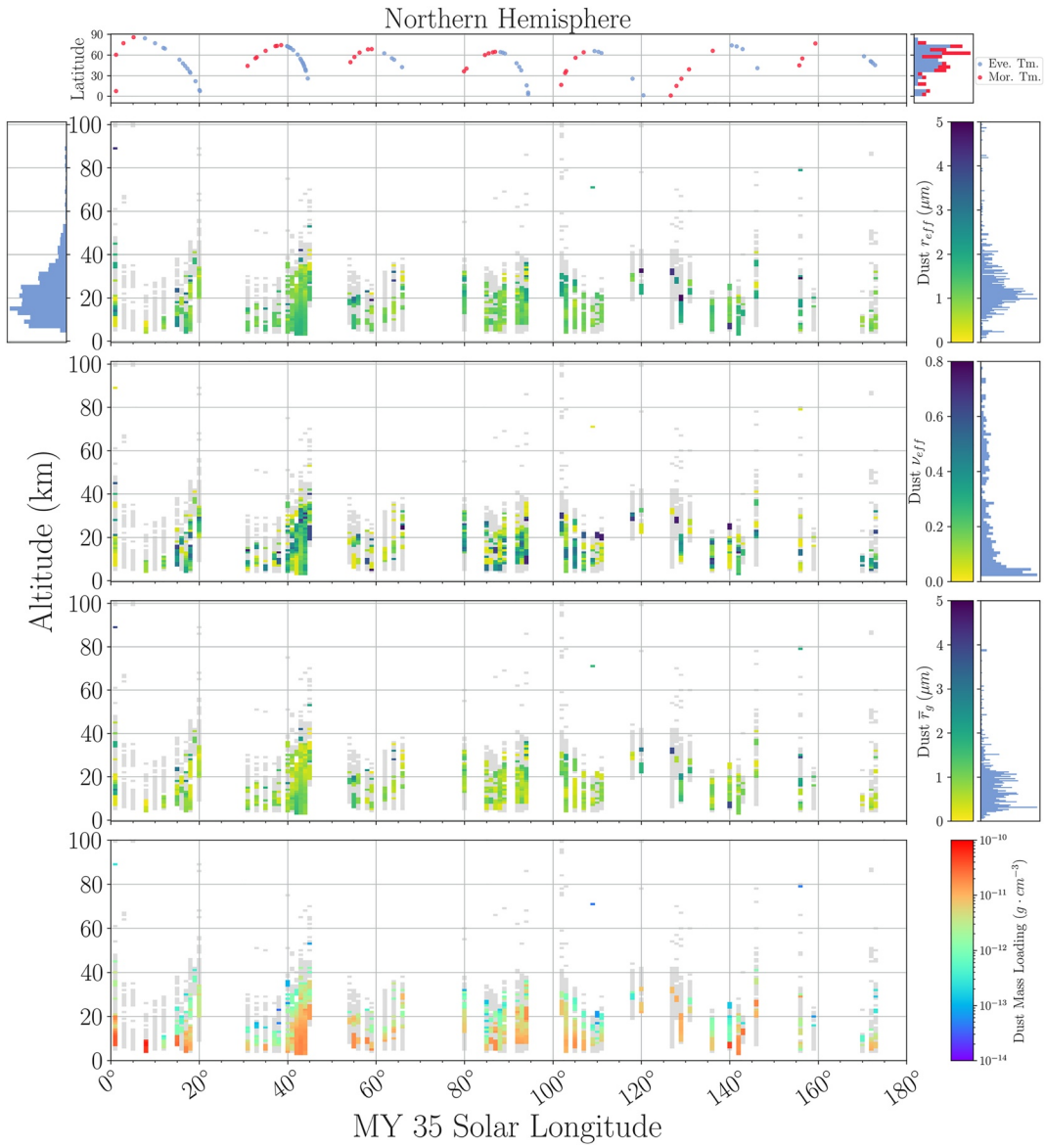

Figure 17. Results of the aerosol distribution properties analysis scheme for dust in the northern hemisphere during the first half of MY 35. The filtered points (high merit function or low/high effective variance) are shown in light gray. All histograms' panels are relative occurrences and share the vertical axis with their relevant parameters.

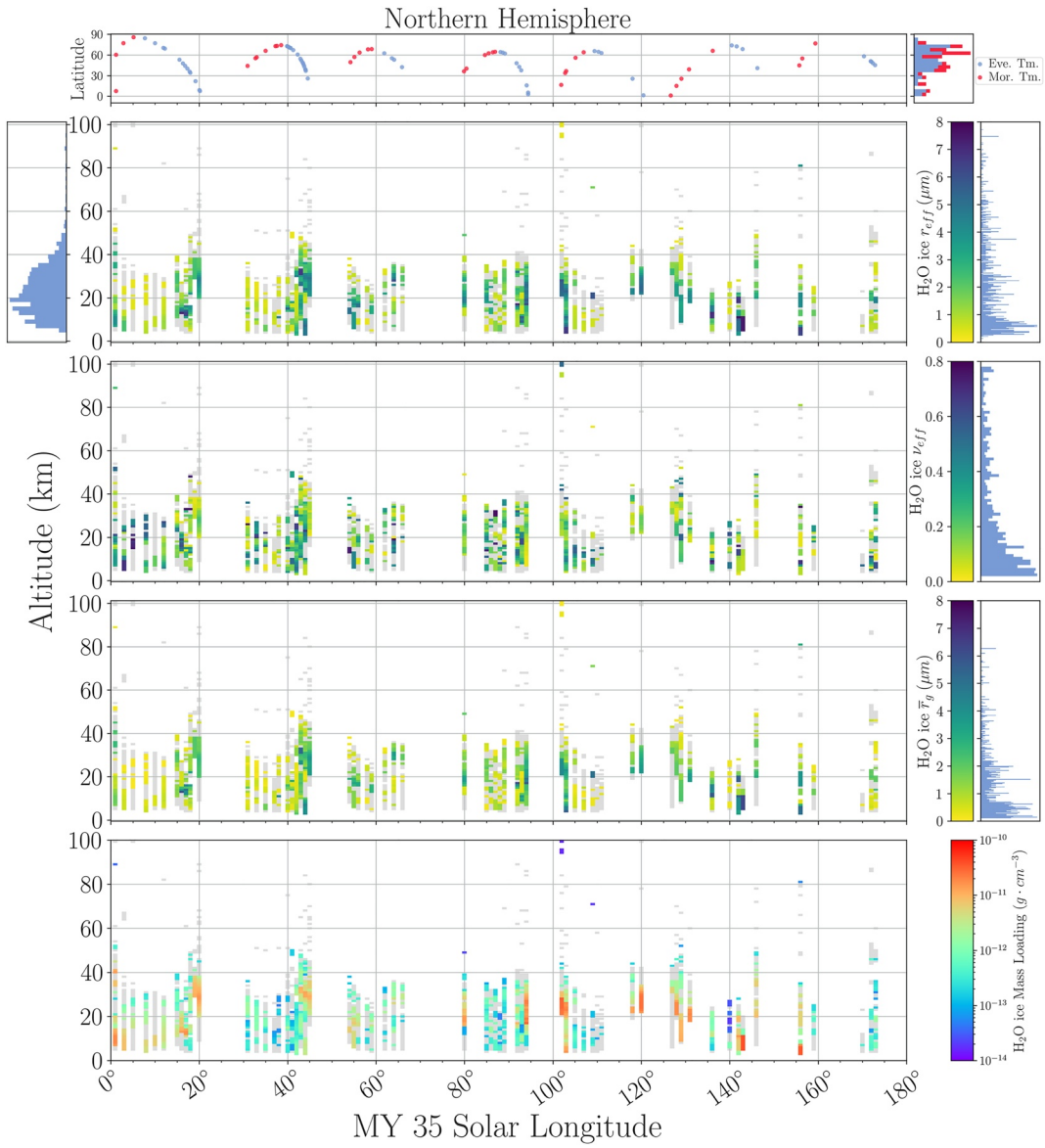

Figure 18. Results of the aerosol distribution properties analysis scheme for H_2O_{ice} in the northern hemisphere during the first half of MY 35. The filtered points (high merit function or low/high effective variance) are shown in light gray). All histograms' panels are relative occurrences and share the vertical axis with their relevant parameters.

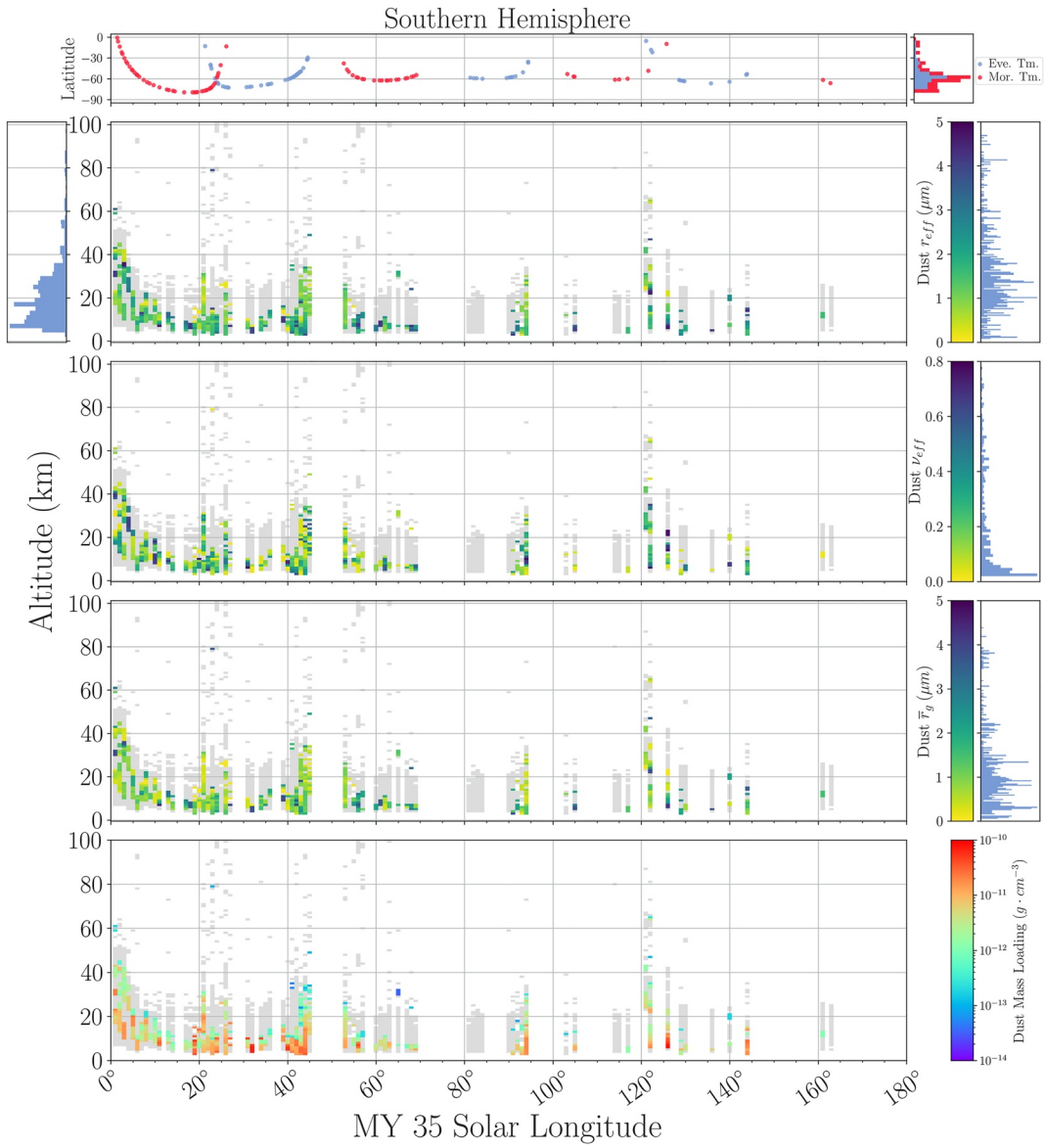

Figure 19. Results of the aerosol distribution properties analysis scheme for dust in the southern hemisphere during the first half of MY 35. The filtered points (high merit function or low/high effective variance) are shown in light gray). All histograms' panels are relative occurrences and share the vertical axis with their relevant parameters.

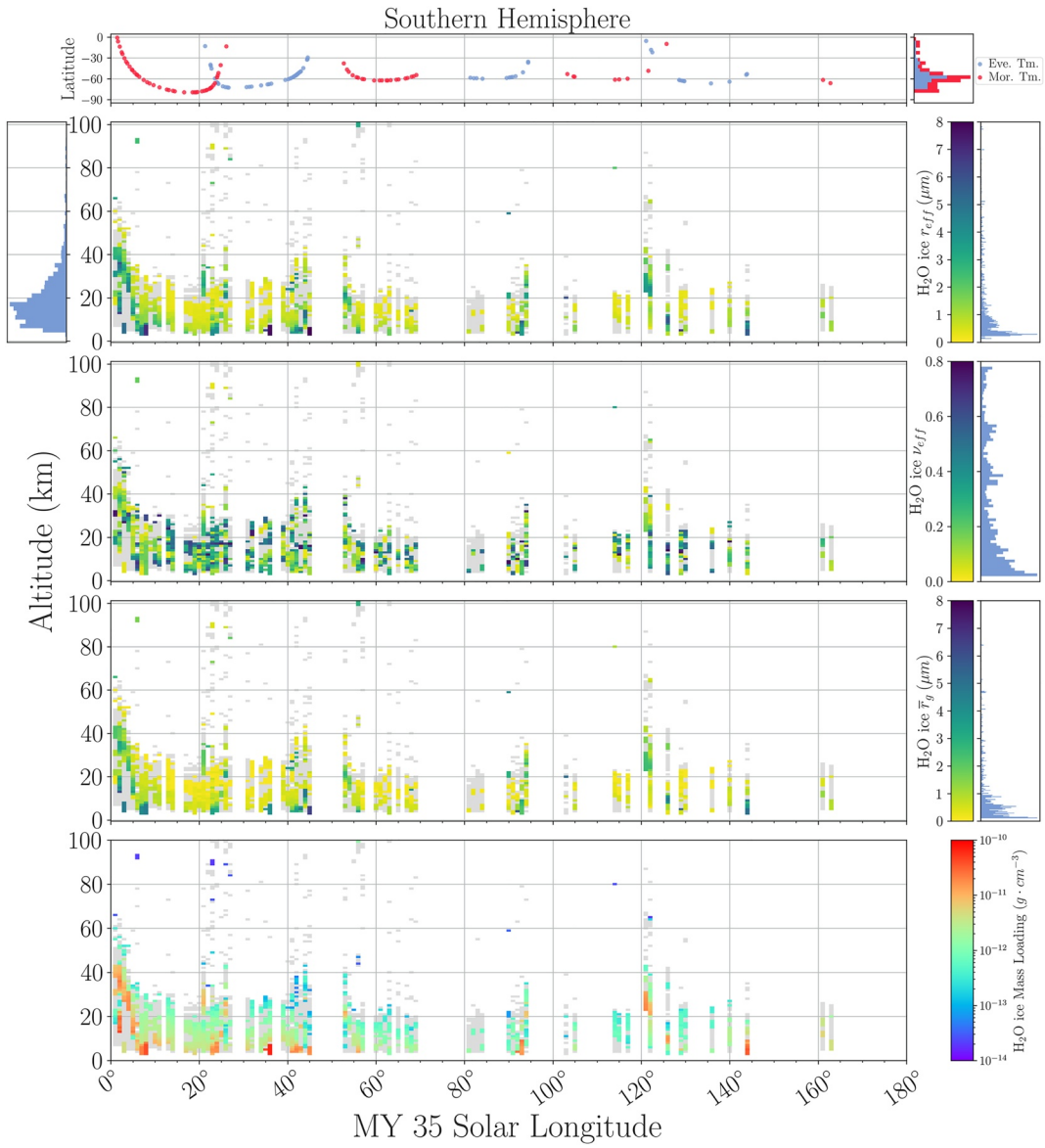

Figure 20. Results of the aerosol distribution properties analysis scheme for H_2O_{ice} in the southern hemisphere during the first half of MY 35. The filtered points (high merit function or low/high effective variance) are shown in light gray. All histograms panels are relative occurrences and share the vertical axis with their relevant parameters.

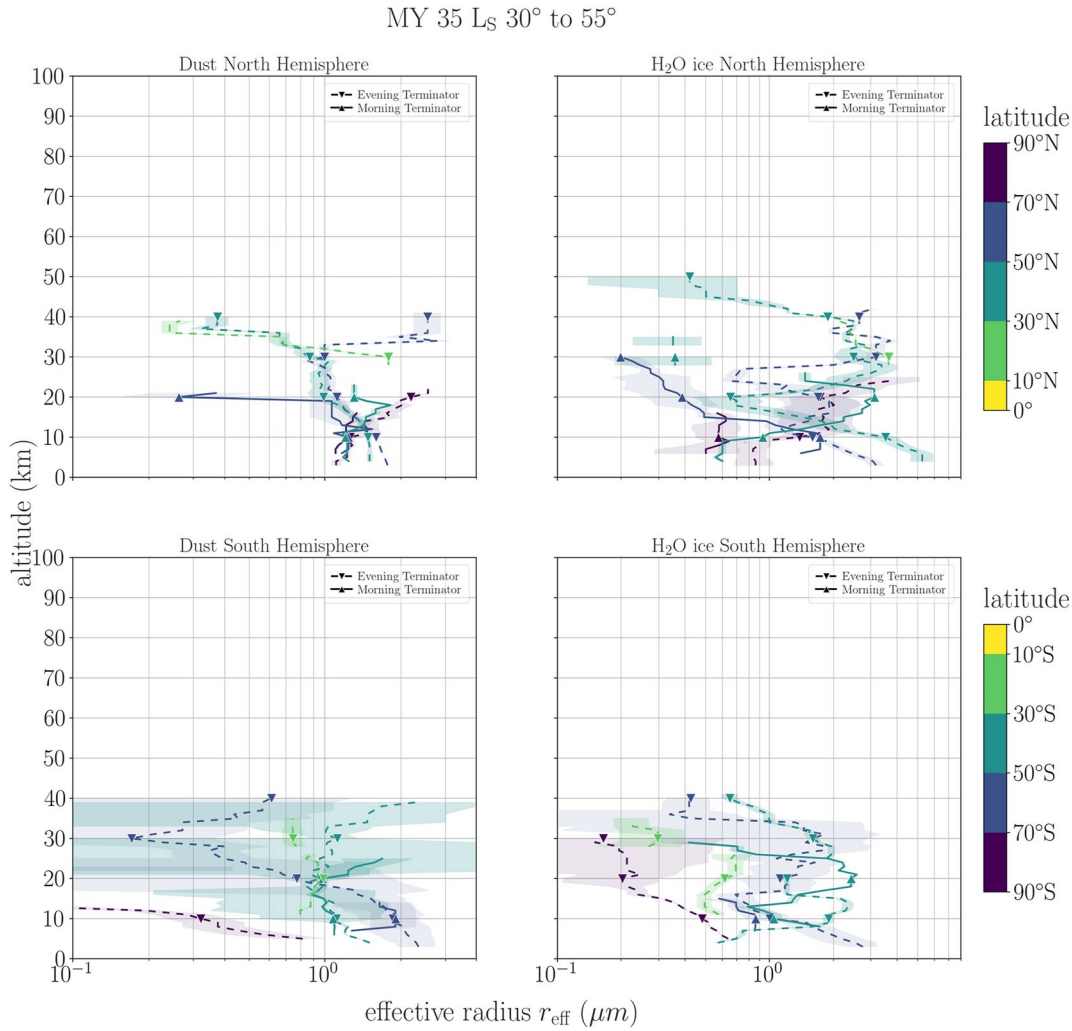

Figure 21. Latitudinal panels of vertical profiles of the effective radius during the early dust event of MY 35. Blue represent H_2O_{ice}. Red represent dust. Diamonds and stars stand for morning and evening terminators respectively.

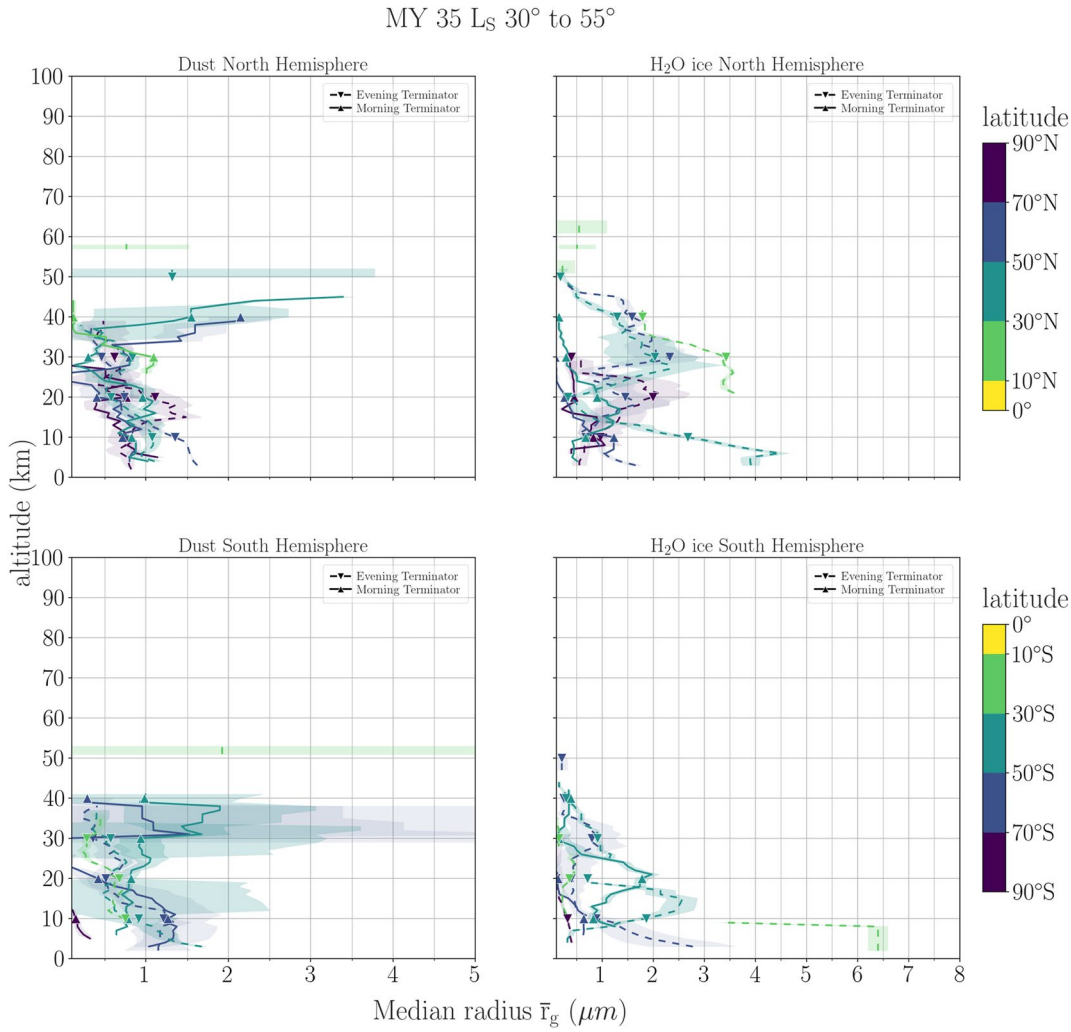

Figure 22. Vertical profiles of the median radius during early dust event of MY 35. The vertical profiles are derived from a vertical running average using a vertical window of 10 km. The error displayed by the colored area is the greatest value between the standard deviation of the data points and the error evaluated during the running average.

Data Availability Statement

The results data from our inversion of NOMAD-SO data (extinction profiles) and aerosol fitting procedure, r_{eff}, ν_{eff},γ and their derivatives, are being archived and available from [Dataset] Stolzenbach (2023).

Acknowledgments
Authors Aurélien Stolzenbach, Miguel-Angel López Valverde, Adrian Brines, Ashimananda Modak, Bernd Funke and Francisco González-Galindo acknowledges financial support from the Severo Ochoa Grant CEX2021-001131-S funded by MCIN/AEI/10.13039/501100011033. F. Gonzalez-Galindo is also funded by the Spanish Ministerio de Cieincia, Innovaciòn y Universidades, the Agencia Estatal de Investigaciòn and EC FEDER funds under project RTI2018-100920-J-100. B. Funke also acknowledges support by project PID2019-110689Rb-100/AEI/10.13039/501100011033. ExoMars is a space mission of the European Space Agency (ESA) and Roscosmos. The NOMAD experiment is led by the Royal Belgian Institute for Space Aeronomy (IASB-BIRA), assisted by Co-PI teams from Spain (IAA-CSIC), Italy (INAF-IAPS), and the United Kingdom (Open University). This project acknowledges funding by the Belgian Science Policy Office (BELSPO), with the financial and contractual coordination by the ESA Prodex Office (PEA 4000103401, 4000121493) as well as by UK Space Agency through Grants ST/V002295/1, ST/V005332/1, and ST/S00145X/1 and Italian Space Agency through Grant 2018-2-HH.0. This work was supported by the Belgian Fonds de la Recherche Scientifique—FNRS under Grant 30442502 (ET_HOME). This project has received funding from the European Union's Horizon 2020 research and innovation program under grant agreement No 101004052 (RoadMap project). US investigators were supported by the National Aeronautics and Space Administration. We want to thank the LMD/IPSL and LATMOS/IPSL teams for the continuous development of the Mars PCM. We would like to thank Alexandre Kling (NASA Ames) and the anonymous reviewer whose detailed comments on the structure and scientific content of this article were of great help to us during the review process.

References

Aoki, S., Vandaele, A. C., Daerden, F., Villanueva, G. L., Liuzzi, G., Thomas, I. R., et al. (2019). Water vapor vertical profiles on Mars in dust storms observed by TGO/NOMAD. *Journal of Geophysical Research: Planets*, *124*(12), 3482–3497. https://doi.org/10.1029/2019JE006109

Clancy, R. T., Grossman, A. W., Wolff, M. J., James, P. B., Rudy, D. J., Billawala, Y. N., et al. (1996). Water vapor saturation at low altitudes around Mars Aphelion: A key to Mars climate? *Icarus*, *122*(1), 36–62. https://doi.org/10.1006/icar.1996.0108

Clancy, R. T., Montmessin, F., Benson, J., Daerden, F., Colaprete, A., & Wolff, M. J. (2017). Mars clouds. In F. Forget, M. D. Smith, R. T. Clancy, R. W. Zurek, & R. M. Haberle (Eds.), *The atmosphere and climate of Mars* (pp. 76–105). Cambridge University Press. https://doi.org/10.1017/9781139060172.005

Clancy, R. T., Sandor, B. J., Wolff, M. J., Christensen, P. R., Smith, M. D., Pearl, J. C., et al. (2000). An intercomparison of ground-based millimeter, MGS TES, and Viking atmospheric temperature measurements: Seasonal and interannual variability of temperatures and dust loading in the global Mars atmosphere. *Journal of Geophysical Research*, *105*(E4), 9553–9571. https://doi.org/10.1029/1999JE001089

Clancy, R. T., Wolff, M. J., & Christensen, P. R. (2003). Mars aerosol studies with the MGS TES emission phase function observations: Optical depths, particle sizes, and ice cloud types versus latitude and solar longitude. *Journal of Geophysical Research*, *108*(E9), 5098. https://doi.org/10.1029/2003JE002058

Clancy, R. T., Wolff, M. J., Smith, M. D., Kleinböhl, A., Cantor, B. A., Murchie, S. L., et al. (2019). The distribution, composition, and particle properties of Mars mesospheric aerosols: An analysis of CRISM visible/near-IR limb spectra with context from near-coincident MCS and MARCI observations. *Icarus*, *328*, 246–273. https://doi.org/10.1016/j.icarus.2019.03.025

Clancy, R. T., Wolff, M. J., Whitney, B. A., Cantor, B. A., Smith, M. D., & McConnochie, T. H. (2010). Extension of atmospheric dust loading to high altitudes during the 2001 Mars dust storm: MGS TES limb observations. *Icarus*, *207*(1), 98–109. https://doi.org/10.1016/j.icarus.2009.10.011

Davies, D. W. (1979). Effects of dust on the heating of Mars' Surface and atmosphere. *Journal of Geophysical Research*, *84*(B14), 8289–8293. https://doi.org/10.1029/JB084iB14p08289

Fedorova, A. A., Montmessin, F., Korablev, O., Luginin, M., Trokhimovskiy, A., Belyaev, D. A., et al. (2020). Stormy water on Mars: The distribution and saturation of atmospheric water during the dusty season. *Science*, *367*(6475), 297–300. https://doi.org/10.1126/science.aay9522

Forget, F., Hourdin, F., Fournier, R., Hourdin, C., Talagrand, O., Collins, M., et al. (1999). Improved general circulation models of the Martian atmosphere from the surface to above 80 km. *Journal of Geophysical Research*, *104*(E10), 24155–24175. https://doi.org/10.1029/1999je001025

Guzewich, S. D., Lemmon, M., Smith, C. L., Martínez, G., de Vicente-Retortillo, A., Newman, C. E., et al. (2019). Mars science laboratory observations of the 2018/Mars Year 34 global dust storm. *Geophysical Research Letters*, *46*(1), 71–79. https://doi.org/10.1029/2018GL080839

Guzewich, S. D., & Smith, M. D. (2019). Seasonal variation in Martian water ice cloud particle size. *Journal of Geophysical Research: Planets*, *124*(2), 636–643. https://doi.org/10.1029/2018JE005843

Guzewich, S. D., Smith, M. D., & Wolff, M. J. (2014). The vertical distribution of Martian aerosol particle size. *Journal of Geophysical Research: Planets*, *119*(12), 2694–2708. https://doi.org/10.1002/2014JE004704

Haberle, R. M., Clancy, R. T., Forget, F., Smith, M. D., & Zurek, R. W. (Eds.) (2017). *The atmosphere and climate of Mars*. Cambridge University Press. https://doi.org/10.1017/9781139060172

Holmes, J. A., Lewis, S. R., Patel, M. R., Chaffin, M. S., Cangi, E. M., Deighan, J., et al. (2021). Enhanced water loss from the Martian atmosphere during a regional-scale dust storm and implications for long-term water loss. *Earth and Planetary Science Letters*, *571*, 117109. https://doi.org/10.1016/j.epsl.2021.117109

James, P. B., Bell, J. F., III., Clancy, R. T., Lee, S. W., Martin, L. J., & Wolff, M. J. (1996). Global imaging of Mars by Hubble space telescope during the 1995 opposition. *Journal of Geophysical Research*, *101*(E8), 18883–18890. https://doi.org/10.1029/96JE01605

Kahre, M. A., Murphy, J. R., Newman, C. E., Wilson, R. J., Cantor, B. A., Lemmon, M. T., & Wolff, M. J. (2017). The Mars dust cycle. In F. Forget, M. D. Smith, R. T. Clancy, R. W. Zurek, & R. M. Haberle (Eds.), *The atmosphere and climate of Mars* (pp. 295–337). Cambridge University Press. https://doi.org/10.1017/9781139060172.010

Kass, D. M., Kleinboehl, A., Shirley, J. H., & Cantor, B. A. (2020). In *Observations of the Mars Year 35 E (Early) large-scale regional dust event*. (Vol. 2020). (Conference Name: AGU Fall Meeting Abstracts ADS Bibcode: 2020AGUFMP039…01K) Retrieved from https://ui.adsabs.harvard.edu/abs/2020AGUFMP039…01K

Kass, D. M., Kleinböhl, A., McCleese, D. J., Schofield, J. T., & Smith, M. D. (2016). Interannual similarity in the Martian atmosphere during the dust storm season. *Geophysical Research Letters*, *43*(12), 6111–6118. https://doi.org/10.1002/2016GL068978

Kleinböhl, A., Schofield, J. T., Abdou, W. A., Irwin, P. G. J., & de Kok, R. J. (2011). A single-scattering approximation for infrared radiative transfer in limb geometry in the Martian atmosphere. *Journal of Quantitative Spectroscopy and Radiative Transfer*, *112*(10), 1568–1580. https://doi.org/10.1016/j.jqsrt.2011.03.006

Kleinböhl, A., Schofield, J. T., Kass, D. M., Abdou, W. A., Backus, C. R., Sen, B., et al. (2009). Mars Climate Sounder limb profile retrieval of atmospheric temperature, pressure, and dust and water ice opacity. *Journal of Geophysical Research*, *114*(E10), E10006. https://doi.org/10.1029/2009JE003358

Korablev, O., Moroz, V. I., Petrova, E. V., & Rodin, A. V. (2005). Optical properties of dust and the opacity of the Martian atmosphere. *Advances in Space Research*, *35*(1), 21–30. https://doi.org/10.1016/j.asr.2003.04.061

Liuzzi, G., Villanueva, G. L., Crismani, M. M., Smith, M. D., Mumma, M. J., Daerden, F., et al. (2020). Strong variability of Martian water ice clouds during dust storms revealed from ExoMars Trace Gas Orbiter/NOMAD. *Journal of Geophysical Research: Planets*, *125*(4), e2019JE006250. https://doi.org/10.1029/2019JE006250

López Valverde, M.-A., Funke, B., Brines, A., Stolzenbach, A., Modak, A., Hill, B., et al. (2022). Martian atmospheric temperature and density profiles during the 1st year of NOMAD/TGO solar occultation measurements. *Journal of Geophysical Research: Planets*, e2022JE007278. https://doi.org/10.1029/2022JE007278

Luginin, M., Fedorova, A., Ignatiev, N., Trokhimovskiy, A., Shakun, A., Grigoriev, A., et al. (2020). Properties of water ice and dust particles in the atmosphere of Mars during the 2018 global dust storm as inferred from the atmospheric chemistry suite. *Journal of Geophysical Research: Planets*, *125*(11), e2020JE006419. https://doi.org/10.1029/2020JE006419

Madeleine, J.-B., Forget, F., Spiga, A., Wolff, M. J., Montmessin, F., Vincendon, M., et al. (2012). Aphelion water-ice cloud mapping and property retrieval using the OMEGA imaging spectrometer onboard Mars Express. *Journal of Geophysical Research*, *117*(E11), E00J07. https://doi.org/10.1029/2011JE003940

McCleese, D. J., Heavens, N. G., Schofield, J. T., Abdou, W. A., Bandfield, J. L., Calcutt, S. B., et al. (2010). Structure and dynamics of the Martian lower and middle atmosphere as observed by the Mars Climate Sounder: Seasonal variations in zonal mean temperature, dust, and water ice aerosols. *Journal of Geophysical Research*, *115*(E12), E12016. https://doi.org/10.1029/2010JE003677

Montabone, L., Forget, F., Millour, E., Wilson, R. J., Lewis, S. R., Cantor, B., et al. (2015). Eight-year climatology of dust optical depth on Mars. *Icarus*, *251*, 65–95. https://doi.org/10.1016/j.icarus.2014.12.034

Montmessin, F., Forget, F., Rannou, P., Cabane, M., & Haberle, R. M. (2004). Origin and role of water ice clouds in the Martian water cycle as inferred from a general circulation model. *Journal of Geophysical Research*, *109*(E10). https://doi.org/10.1029/2004JE002284

Montmessin, F., Korablev, O., Lefèvre, F., Bertaux, J. L., Fedorova, A., Trokhimovskiy, A., et al. (2017). SPICAM on Mars Express: A 10 year in-depth survey of the Martian atmosphere. *Icarus*, *297*, 195–216. https://doi.org/10.1016/j.icarus.2017.06.022

Navarro, J., & Aythami, A. (2016). *Retrieval of CO_2 and collisional parameters from the MIPAS spectra in the earth atmosphere*. Universidad de Granada. Retrieved from https://digibug.ugr.es/handle/10481/41725

Navarro, T., Forget, F., Millour, E., & Greybush, S. J. (2014). Detection of detached dust layers in the Martian atmosphere from their thermal signature using assimilation. *Geophysical Research Letters*, *41*(19), 6620–6626. https://doi.org/10.1002/2014GL061377

Richardson, M. I., & Wilson, R. J. (2002). Investigation of the nature and stability of the Martian seasonal water cycle with a general circulation model. *Journal of Geophysical Research*, *107*(E5), 7-1–7-28. https://doi.org/10.1029/2001JE001536

Rodgers, C. D. (2000). *Inverse methods for atmospheric sounding*. WORLD SCIENTIFIC. https://doi.org/10.1142/3171

Smith, M. D. (2004). Interannual variability in TES atmospheric observations of Mars during 1999–2003. *Icarus*, *167*(1), 148–165. https://doi.org/10.1016/j.icarus.2003.09.010

Smith, M. D. (2009). THEMIS observations of Mars aerosol optical depth from 2002–2008. *Icarus*, *202*(2), 444–452. https://doi.org/10.1016/j.icarus.2009.03.027

Smith, M. D., Wolff, M. J., Clancy, R. T., Kleinböhl, A., & Murchie, S. L. (2013). Vertical distribution of dust and water ice aerosols from CRISM limb-geometry observations. *Journal of Geophysical Research: Planets*, *118*(2), 321–334. https://doi.org/10.1002/jgre.20047

Stcherbinine, A., Montmessin, F., Vincendon, M., Wolff, M. J., Vals, M., Korablev, O., et al. (2022). A two Martian Years survey of water ice clouds on Mars with ACS onboard TGO. *Journal of Geophysical Research: Planets*, *127*(12), e2022JE007502. https://doi.org/10.1029/2022JE007502

Stcherbinine, A., Vincendon, M., Montmessin, F., Wolff, M. J., Korablev, O., Fedorova, A., et al. (2020). Martian water ice clouds during the 2018 global dust storm as observed by the ACS-MIR channel onboard the trace gas orbiter. *Journal of Geophysical Research: Planets*, *125*(3), e2019JE006300. https://doi.org/10.1029/2019JE006300

Stiller, G. P., Hoepfner, M., Kuntz, M., von Clarmann, T., Echle, G., Fischer, H., et al. (1998). Karlsruhe optimized and precise radiative transfer algorithm: I. Requirements, justification, and model error estimation. In J. Wang, B. Wu, T. Ogawa, & Z. hua Guan (Eds.), *Optical remote sensing of the atmosphere and clouds* (Vol. 3501, pp. 257–268). SPIE. https://doi.org/10.1117/12.317754

Stolzenbach, A. (2023). ADS v4 results for MY 34 & 35 [Dataset]. Zenodo. https://doi.org/10.5281/zenodo.7753821

Stolzenbach, A., Valverde, M.-A. L., Brines, A., Modak, A., Funke, B., González-Galindo, F., et al. (2023). Martian atmospheric aerosols composition and distribution retrievals during the first Martian year of NOMAD/TGO solar occultation measurements. Part I: Methodology and application to the MY 34 global dust storm. *Journal of Geophysical Research: Planets*, *128*, e2022JE007276. https://doi.org/10.1029/2022JE007276

Vandaele, A. C., Lopez-Moreno, J.-J., Patel, M. R., Bellucci, G., Daerden, F., Ristic, B., et al. (2018). NOMAD, an integrated suite of three spectrometers for the ExoMars Trace Gas Mission: Technical description, science objectives and expected performance. *Space Science Reviews*, *214*(5), 80. https://doi.org/10.1007/s11214-018-0517-2

Wilson, R. J., Lewis, S. R., Montabone, L., & Smith, M. D. (2008). Influence of water ice clouds on Martian tropical atmospheric temperatures. *Geophysical Research Letters*, *35*(7), L07202. https://doi.org/10.1029/2007GL032405

Wolff, M. J., & Clancy, R. T. (2003). Constraints on the size of Martian aerosols from thermal emission spectrometer observations. *Journal of Geophysical Research*, *108*(E9), 5097. https://doi.org/10.1029/2003JE002057

Wolff, M. J., Lopéz-Valverde, M., Madeleine, J.-B., Wilson, R. J., Smith, M. D., Fouchet, T., & Delory, G. T. (2017). Radiative process: Techniques and applications. In F. Forget, M. D. Smith, R. T. Clancy, R. W. Zurek, & R. M. Haberle (Eds.), *The atmosphere and climate of Mars* (pp. 106–171). Cambridge University Press. https://doi.org/10.1017/9781139060172.006

Wolff, M. J., Smith, M. D., Clancy, R. T., Spanovich, N., Whitney, B. A., Lemmon, M. T., et al. (2006). Constraints on dust aerosols from the Mars exploration rovers using MGS overflights and Mini-TES. *Journal of Geophysical Research*, *111*(E12), E12S17. https://doi.org/10.1029/2006JE002786

Zurek, R. W., & Martin, L. J. (1993). Interannual variability of planet-encircling dust storms on Mars. *Journal of Geophysical Research*, *98*(E2), 3247–3259. https://doi.org/10.1029/92je02936